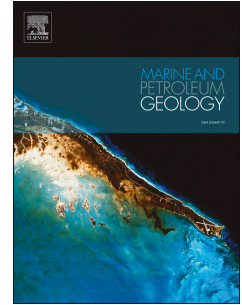


# Accepted Manuscript

Continuous porosity characterization: Metric-scale intervals in heterogeneous sedimentary rocks using medical CT-scanner

Stéphanie Larmagnat, Mathieu Des Roches, Louis-Frédéric Daigle, Pierre Francus, Denis Lavoie, Jasmin Raymond, Michel Malo, Alexandre Aubiès-Trouilh



PII: S0264-8172(19)30189-8

DOI: <https://doi.org/10.1016/j.marpetgeo.2019.04.039>

Reference: JMPG 3818

To appear in: *Marine and Petroleum Geology*

Received Date: 15 December 2018

Revised Date: 31 March 2019

Accepted Date: 30 April 2019

Please cite this article as: Larmagnat, Sté., Des Roches, M., Daigle, Louis.-Fré., Francus, P., Lavoie, D., Raymond, J., Malo, M., Aubiès-Trouilh, A., Continuous porosity characterization: Metric-scale intervals in heterogeneous sedimentary rocks using medical CT-scanner, *Marine and Petroleum Geology* (2019), doi: <https://doi.org/10.1016/j.marpetgeo.2019.04.039>.

This is a PDF file of an unedited manuscript that has been accepted for publication. As a service to our customers we are providing this early version of the manuscript. The manuscript will undergo copyediting, typesetting, and review of the resulting proof before it is published in its final form. Please note that during the production process errors may be discovered which could affect the content, and all legal disclaimers that apply to the journal pertain.

1 **CONTINUOUS POROSITY CHARACTERIZATION:**  
2 **METRIC-SCALE INTERVALS IN HETEROGENEOUS SEDIMENTARY**  
3 **ROCKS USING MEDICAL CT-SCANNER**

4

5 Stéphanie Larmagnat<sup>1</sup>, Mathieu Des Roches<sup>2</sup>, Louis-Frédéric Daigle<sup>2</sup>, Pierre Francus<sup>2</sup>,  
6 Denis Lavoie<sup>1</sup>, Jasmin Raymond<sup>2</sup>, Michel Malo<sup>2</sup>, Alexandre Aubiès-Trouilh<sup>3</sup>

7

8 <sup>1</sup> Geological Survey of Canada, 490, rue de la Couronne, Québec (Québec), Canada, G1K 9A9  
9 stephanie.larmagnat@canada.ca

10 <sup>2</sup> INRS - Centre ETE, 490, rue de la Couronne, Québec (Québec), Canada, G1K 9A9

11 <sup>3</sup> Ressources & Énergie Squatex Inc., 7055, boul. Taschereau, bureau 500, Brossard, Canada, G1Z 1A7

12

13

14 **Abstract**

15 Although computed tomography (CT-Scanning) has been regularly applied to core  
16 analyses in petroleum geology, there is still a need to improve our ways to document  
17 porosity and porosity distribution in the entire pore scale spectrum, from the tens of  
18 nanometer to the meter-scale. Porosity imaging is particularly crucial for complex and  
19 heterogeneous rocks such as hydrothermally altered and fractured carbonates. The present  
20 work proposes a improved method using medical-CT to reliably estimate reservoir  
21 porosity. An in-house core-flooding setup allowed to analyse several individual core  
22 samples, scanned simultaneously (dry and saturated), as well as continuous core sections  
23 up to 1.5 m long. Without any prior knowledge of samples, three-dimensional alignment  
24 and subtraction of the two data sets (dry and saturated states) results in the generation of  
25 3D porosity matrices. The methodology tested on a large set of reference core material  
26 shows a strong correlation between conventional gas porosimetry techniques and porosity  
27 from CT-scan. The added value of the porosity measurements by CT-scan is, first of all,  
28 the generation of 3D images of pore network, allowing to assess spatial attributes of  
29 macropores, their distribution and connectivity. Secondly, the CT-scan method also  
30 provides continuous porosity profile at the millimetric scale. Both developments are  
31 crucial for the understanding of reservoir rock properties.

32 **Keywords:** 3D porosity, carbonate, core-flooding, CT scan

33

34 **INTRODUCTION**

35 The spatial distribution of petrophysical properties of reservoir rocks commonly needs to  
36 be assessed whether it is for the exploration of hydrocarbons, the identification of  
37 efficient reservoir for CO<sub>2</sub> storage or the assessment of geothermal resources (e.g.  
38 Kukkonen and Peltoniemi, 1998; Mees et al., 2003; Chadwick et al., 2004; Hartmann et  
39 al., 2008; Shi et al., 2009; Goldberg et al., 2010; Perrin and Benson, 2010a). Computed  
40 tomography (CT-scanning) has been applied for decades by the hydrocarbon community  
41 to supplement conventional core analyses (such as mineralogy, porosity, permeability) or  
42 wireline logging interpretation (Vinegar and Wellington, 1987; Wellington and Vinegar,  
43 1987; Dulu, 1999; Akin and Kovsky, 2003; Taud et al., 2005; Geiger et al., 2009;  
44 Baniak et al., 2013). CT-scanning techniques are non-destructive and offer the possibility  
45 to quantify internal structures based on the measurement of X-Rays attenuation  
46 coefficients, which depend on the chemical composition and physical density of the  
47 materials analysed (Dulu, 1999; Akin and Kovsky, 2003; Cnudde and Boone, 2013).  
48 Therefore, CT-scanning provides qualitative analysis when applied to subsurface  
49 materials (e.g. heterogeneity, damages, presence of fluids); it can also be used to gain  
50 quantitative information on cores such as bulk density, porosity, and fluid saturations  
51 (Coles et al., 1991; Cnudde and Boone, 2013). Efforts have also been made to use CT-  
52 scanning to understand fluid displacement and relative permeability of core material from  
53 reservoirs (Hove et al., 1987; Vinegar and Wellington, 1987; Withjack, 1988), notably  
54 because of their importance in oil-recovery processes during production stages  
55 (Andrianov et al., 2012; Simjoo et al., 2013; Simjoo and Zitha, 2018). Limitations of  
56 medical CT (or conventional CT, as proposed by Ketcham and Carlson (2001) ) are well

57 known. The image spatial resolution obtained is relatively low (about 0.5 mm on  
58 average), allowing characterization and quantification of the spatial distribution of larger  
59 structures only such as burrows, roots, primary or secondary framework pores or  
60 fractures. The use of medical CT systems is consequently being complemented by  
61 MicroCT and synchrotron based systems (Ketcham and Carlson, 2001; Cnudde and  
62 Boone, 2013; Wildenschild and Sheppard, 2013) that offers a better resolution.

63 However, there is a critical need to get data on the entire pore scale spectrum, from the  
64 tens of nanometer to the meter-scale in order to build comprehensive datasets for rocks,  
65 sediments and soils (Okabe and Blunt, 2007; Biswal et al., 2009; Vaz et al., 2014;  
66 Bultreys et al., 2016b; Xiong et al., 2016). Porosity imaging and pore-network modelling  
67 techniques are crucial for characterizing complex and heterogeneous rocks such as  
68 carbonates (Sok et al., 2010; Pak et al., 2016). Deposition processes and diagenesis result  
69 into heterogeneity at multiple spatial scales so that predicting petrophysical properties is  
70 particularly challenging in carbonate reservoir rocks. Pore structure affects connectivity,  
71 conductivity and permeability that all influence oil recovery mechanisms, a key aspect for  
72 economic geology. MicroCT and synchrotron-based systems give access to spatial  
73 resolutions of few micrometers to deal with pore-particles interfaces but sample size is  
74 restricted to few millimeters (Vaz et al., 2014) and is time-consuming. The trade-off  
75 between sample size and spatial resolution (i.e. voxel size), mainly imposed by the micro-  
76 CT scanner detector characteristics, is therefore a limitation to upscale data obtained at  
77 the pore scale and justifies modelling. Even if significant developments are made  
78 regarding small scale heterogeneity characterization techniques, there is a need to

79 optimize characterisation of heterogeneous material such as fractured or dolomitized  
80 carbonates at the centimeter scale.

81 Coupled with core-flooding experiments, CT scanning are well establish in reservoir  
82 studies to monitor the progress of multiphase displacement inside porous media  
83 (Schembre and Kovscek, 2003; Shi et al., 2009). Different core-flooding setups exist,  
84 depending on the fluids involved or the experimental conditions, such as the confining  
85 pressure that can be radial and/or axial, the temperature (reservoir condition), or the fluid  
86 injection mode (Wang et al., 1984; Alemu et al., 2013). The reliability of such scanning  
87 technique was verified through a study of oil and gas shows in eastern Québec, where an  
88 industry, university and government partnership was developed to improve current CT  
89 scan methods, which remained difficult to use when characterizing reservoir properties in  
90 heterogeneous carbonates. The authors found, to the extent of their knowledge, that  
91 rigorous and complete scientific literature on CT scan technique was needed to  
92 implement a detailed characterization program with specific interest to carbonate rocks.  
93 Studied rock units were locally found within highly fractured intervals associated with  
94 replacive and pore-filing hydrothermal dolomites. The industry partner, Squatex Inc.,  
95 drilled and cored over 6000 m of stratigraphic exploration wells and needed an efficient  
96 and rapid way to assess the spatial distribution of reservoir properties in the area in order  
97 to plan their future works.

98 This project objective was to complement and enhance current CT scan methods applied  
99 to sedimentary rocks in order to reliably document porosity distribution and connectivity  
100 in heterogeneous carbonate reservoirs and to predict its distribution over a metric scale.  
101 An improved methodology combining a core-flooding setup and medical-CT analyses to

102 obtain the porosity of heterogeneous rock material was consequently developed. No  
103 confinement pressure is applied during saturation: water flows around sample and the  
104 experiment is conducted at room temperature. The methodology has been tested on  
105 reference core material that has a wide range of porosity values and includes eight  
106 different sedimentary rock types. To test this enhanced CT methodology, porosity results  
107 are compared with conventional ways to determine porosity in rock material (i.e. helium  
108 gas porosimetry). In addition, the methodology was tested on a specific metric section of  
109 an heterogeneous carbonate interval. Within this interval, 3D porosity matrices were  
110 generated to visualize the connected porosity network, as well as a continuous porosity  
111 profiles at the millimetric scale.

## 112 **PREVIOUS WORKS**

### 113 1) CT-scanning

114 Both medical and microfocus CT-scanning (Micro-CT) has been commonly used for  
115 decades for core analyses in the Oil and Gas sector in order to analyse porosity, fractures  
116 patterns, or assess fluid flow in porous rocks (e.g. Honarpour et al., 1985; Grader et al.,  
117 2000; Van Geet and Swennen, 2001; Akin and Kovscek, 2003; Karacan et al., 2003; Van  
118 Geet et al., 2003; Denney, 2004; Taud et al., 2005; Geiger et al., 2009). Images generated  
119 contains relative density measurements in Houndsfield Unit (HU) and allow qualitative,  
120 such as internal structures description, and quantitative information analysis. Different  
121 parameters can be derived from HU values as it relates to three physical aspects: real  
122 density, chemical composition (atomic number) and porosity. To isolate each properties,  
123 different methods has been developed. The atomic number can be computed using Dual-  
124 energy scans (Wellington and Vinegar, 1987; Alves et al., 2014; Jussiani and Appoloni,

125 2015). Density estimation in  $\text{g/cm}^3$  is often estimated using calibration points obtained  
126 from core plugs. Finally, porosity is estimated using various approach: (1) segmentation  
127 of pores, (2) mixels (or mixed pixels(Kato et al., 2013) assuming grain density and (3)  
128 saturation technique and subtraction of saturated and dry state (Withjack, 1988; Davis et  
129 al., 1992).

## 130 2) Core-flooding system

131 From the 1950's, hydrocarbon exploration companies have commonly used X-rays to  
132 study reservoir properties (Morgan et al., 1950) and, with the advance of 3D computed  
133 tomography, to visualize fluid flow through reservoir rocks, calculate porosity and oil  
134 saturation (Vinegar and Wellington, 1987; Wellington and Vinegar, 1987; Withjack,  
135 1988). Numerous papers provided excellent syntheses on computed tomography  
136 principles and common practices (e.g. Newton and Potts, 1981; Ketcham and Carlson,  
137 2001). With respect to core flooding experiments, tests under CT are primarily made to  
138 observe fluids displacement and to gain information about relative permeabilities  
139 (e.g. Wang et al., 1984; Hove et al., 1987; Wellington and Vinegar, 1987; Soltani et al.,  
140 2009), either comparing two liquid phases (e.g. oil, brines) or using a gas phase (e.g.  
141  $\text{CO}_2$ ) and a denser liquid phase (Schembre and Kavscek, 2003; Shi et al., 2009; Perrin  
142 and Benson, 2010b; Alemu et al., 2013; Krause et al., 2013; Krause and Benson, 2015;  
143 Jackson et al., 2018). In more recent years, core-flooding studies were carried out with  
144 one sample at the time only and were usually associated with a dynamic set-up, using  
145 pump(s) to ensure constant fluid circulation trough the core holder and samples. Most  
146 common setup involves a water filled chamber made of multi layers sleeve and hosting  
147 the sample. The chamber is maintained at particular confining pressure and temperature

148 in order to reproduce reservoir conditions at depth (Perrin and Benson, 2010a; Krevor et  
149 al., 2012; Pini et al., 2012).

150 In the late 1980's, Withjack (1988) presented a protocol to measure saturation and  
151 porosity with a core-flooding device under CT. This work was based on X-rays and  
152 porosity determination principles recognized years before (Morgan et al., 1950; Laird and  
153 Putnam, 1959). The setup of Withjack (1988) first involved core samples placed in an  
154 aluminium chamber and scanned in a dry state. The aluminum chamber was used to  
155 remove lower-energy photons and limit beam hardening artefacts. Prior to the  
156 experiment, polyethylene bottles filled with sodium iodide solutions were scanned  
157 separately inside the core holder. Then core samples were removed from the chamber, put  
158 under vacuum conditions and immersed in the sodium iodide solution. Once samples  
159 were considered saturated, they were put back in the chamber and scanned under CT.  
160 Withjack (1988) tested a Berea sandstone and a dolomite with both porosity around 20%.  
161 Porosity was also measured by the re-saturation method for comparison purposes.  
162 Although CT-scan capabilities remained limited at that time, Withjack (1988)  
163 demonstrated that CT-scan porosity values correlated well with those obtained by re-  
164 saturation ( $\pm 1$  %). The approach described in this paper is primarily based on the so-  
165 called X-ray saturation technique developed by Withjack (1988) , but includes recent  
166 advances such as procedures for registration and to reduce image noise (e.g. Ketcham and  
167 Iturrino, 2005; Pini et al., 2012; Pini and Madonna, 2016).

168 3) Doping agents used with CT-scan

169 A doping agent is a fluid with dissolved salts having a high atomic number ( $Z \geq 50$ ),  
170 which alters X-rays absorption properties of the fluid phase. This enhances the contrast

171 between solid and fluid phase (Wildenschild et al., 2002). The use of such dopant is  
172 common in the hydrocarbon industry when working on multiphase fluid flow  
173 experiments (e.g. Vinegar and Wellington, 1987), and the most popular choices for  
174 doping brines are sodium bromide (NaBr), sodium molybdate ( $\text{Na}_2\text{MoO}_4$ ) and sodium  
175 iodide (NaI). Doping agents are also widely used in other research areas such as soils  
176 science (Hopmans et al., 1992; Anderson et al., 2003; Helliwell et al., 2013; Vaz et al.,  
177 2014).

178 In the frame of this paper, we present an improved methodology in a sense that we  
179 combine, as simple as it can, a core flooding system that does not require any  
180 confinement. In addition, the setup allows the saturation of multiple meters of samples  
181 simultaneously, thus minimizing the operating cost. In order to validate the methodology,  
182 we studied an extended range of porosity (~1% up to ~30%) and different sedimentary  
183 rock types, including sandstone but with specific interest to dolomite and limestone.

## 184 **METHODOLOGY**

### 185 1) Samples

#### 186 1-1 Reference samples

187 Reference core materials were obtained from two distinct vendors located in the USA:  
188 Cleveland Quarries (Vermilion, Ohio) and Kocurek Industries Inc (Caldwell, Texas).  
189 Eight different lithologies commonly used as test material in the hydrocarbon industry or  
190 rock-mechanics studies were selected (e.g. Churcher et al., 1991; Devarapalli et al., 2017;  
191 Islam et al., 2018). These lithologies were chosen to cover a large range of porosity (1.5  
192 to 28 %; Fig. 1; Tab. 1). All reference core samples are cylindrical and diameter is either

193 3.8 or 4.5 cm. For this work, tested variables therefore include lithology type, porosity  
194 range, core diameter and length.

195 The Berea sandstone is medium-grained, Mississippian in age and outcrops in Ohio  
196 (USA). It is mainly composed of quartz and feldspar with small clay content. Particles are  
197 well sorted and subangular with quartz overgrowths. Berea sandstone is probably the  
198 most commonly used rock as an analogue for hydrocarbon reservoirs (Pini and Madonna,  
199 2016). It has a porosity of approximately 20% (Winkler, 1983; Churcher et al., 1991;  
200 Hart and Wang, 1995; Boon et al., 2017). The Nugget Sandstone is fine-grained,  
201 laminated, Jurassic in age. This sandstone outcrops in Utah and Wyoming (USA). Its  
202 porosity can reach up to 25% (Lindquist, 1988) and it is essentially composed of angular  
203 to subangular quartz grains (Fig. 2A). The Boise sandstone is a medium to coarse-grained  
204 Late Miocene sandstone (Winkler, 1983) from Idaho (USA). This sandstone is poorly  
205 sorted and composed of quartz and feldspar, with minor clay (Fig. 2B). It has a porosity  
206 of approximately 28-30%. The Scioto sandstone is homogenous, fine-grained, Missippian  
207 in age and outcrops in Ohio (USA). Quartz grains are subangular (Figs. 2C-D). This  
208 sandstone commonly has a porosity of approximately 12% (Holder et al., 2001; Bose et  
209 al., 2014). The Indiana limestone, also known as the Salem Formation or the Bedford  
210 limestone, is a middle Mississippian marine bioclastic carbonate that crops out in south-  
211 central Indiana (USA). The limestone is heterogeneous, grainstone to packstone and is  
212 mostly composed of calcium carbonate with only little amount of magnesium carbonate.  
213 Fossil fragments include bryozoans, echinoderms, brachiopods (Churcher et al., 1991).  
214 The Indiana limestone is relatively well cemented and has a porosity of approximately  
215 13% (Musselman, 1967; Schmidt and Huddle, 1977; Hart and Wang, 1995; Boon et al.,

216 2017). The Carthage marble, the commercial name for Carthage limestone or Burlington  
217 limestone, is a homogenous well cemented crinoid-rich Mississippian limestone (Fig. 2E)  
218 that outcrops in Missouri (USA). It is composed predominantly of calcium carbonate with  
219 little amount of glauconite. This limestone exhibits low porosity value, usually about  
220 1.5% (Musselman, 1967; Martin, 1968). The Silurian Dolomite, is a homogeneous fine  
221 grained dolostone in Ohio (USA). It is composed predominantly of non planar dolomite  
222 crystals arranged in mosaic (Fig. 2F) and its porosity is usually around 20%, but could be  
223 down to 14% (e.g. Islam et al., 2018). The Guelph dolomites, also known as the Baker  
224 Dolomite is a homogeneous dolomitized carbonate sand, formed in marine shallow water  
225 environment. Even though two types of Guelph dolomites exist, the samples used in this  
226 work are fine-grained, light gray dolomite (Churcher et al., 1991). The Silurian Guelph  
227 dolomites is present in Ohio (USA) and Ontario (Canada). Its porosity value is usually  
228 around 7% but can be much higher (up to 24%).

#### 229 1-2 Silurian core samples

230 Silurian core samples being studied for this paper come from the Gaspé Belt in Québec  
231 (sensu Bourque et al., 1995) (Fig. 3). It primarily consists of Upper Ordovician to Middle  
232 Devonian fine to coarse nearshore to deep marine clastic deposits with subordinate  
233 shallow- to deep-water carbonate platform deposits. The industry partner, Squatex Inc.  
234 has drilled several stratigraphic wells over the past ten years. Promising reservoir  
235 intervals are located in the cyclic offshore – peritidal carbonates of the lower Silurian  
236 Sayabec Formation and the underlying shoreface clastics of the lower Silurian Val-  
237 Brillant Formation (Lavoie and Bourque, 2001; Lavoie and Morin, 2004). Even if these  
238 two units are not hydrocarbon producers, both have ubiquitous evidence of at least

239 locally, hydrocarbon charge (Lavoie et al., 2009; Dietrich et al., 2011). Hydrothermal  
240 dolomites of the Sayabec Formation are found in the well bedded intertidal to shallow  
241 subtidal facies (Lavoie and Morin, 2004); they host an exhumed oil field a few kilometers  
242 to the east of the study area (Fig. 3) with bitumen and dead oil filling matrix porosity and  
243 fractures (Lavoie and Chi, 2010). While drilling in the Témiscouata area (Fig. 3), oil or  
244 gas shows were associated with naturally fractured hydrothermal dolomites (HTD)  
245 intervals within the Sayabec Formation as well as with the underlying sandstone in the  
246 Val-Brillant Formation. In both cases, the shows seemed to be associated with fractured  
247 intervals (pers. comm., S. Larmagnat, 2015).

248 Silurian samples were recovered from 1 7/8 inch (47.625 mm) diameter drilled cores. All  
249 samples were taken from a specific hydrothermal dolomite interval (Fig. 4A),  
250 corresponding to a section of 1.8 meters long. Due to the lack of integrity of some  
251 portions, only 18 cylindrical core samples with a minimum length of 5 cm have been  
252 selected. Out of this 18 samples set, five samples were sent for helium porosimetry  
253 measurements at an external lab, AGAT Laboratories, after the core-flooding experiment  
254 was completed (Fig. 4B). Those samples were selected on the basis of representability of  
255 the whole 1.8 meter succession. Hence we have selected visually non-porous limestone  
256 muds, limestone mud with some visible pore space, vuggy dolostone, fractured dolostone  
257 and vuggy and fractured dolostone to cover the entire spectrum of depositional/diagenetic  
258 elements present in those carbonates.

259 2) Helium porosity measurements

260 3-1 Reference rock samples

261 Because reference rock samples were not provided with exact porosity values from the  
262 core vendor itself, all reference samples were sent to the external laboratory, namely  
263 AGAT laboratories in Calgary (Canada), to get helium gas porosity measurements.  
264 AGAT Laboratories are private, independent, and routinely run petrophysical properties  
265 analyses (including helium gas porosimetry) for the oil and gas industry, academy and  
266 governmental research teams (e.g. Connell-Madore and Katsube, 2007; Black, 2014;  
267 Gasaway et al., 2018). In addition, depending on sample diameter and length, reference  
268 rock samples were analysed by two additional gas porosimetry instruments at INRS.  
269 From a total of 30 samples, ten samples have been analysed for gas porosimetry by three  
270 distinct instruments and the CT-scanner. All reference samples were analysed at least by  
271 one gas porosimeter and the CT-scanner. In all cases, gas porosity measurements were  
272 conducted on samples before analysing them under the CT-scan.

273 Gas porosity measurements were obtained from instruments relying on Boyle's law: the  
274 pressure exerted by a mass of helium gas is inversely proportional to the volume of the  
275 samples. Measuring the change in helium pressure gives the grain volume. Therefore,  
276 porosity value results from two measurements, grain volume and bulk volume. The first  
277 is measured by the instrument itself and the second is obtained manually using a caliper.  
278 Assuming a perfect cylindrical geometry, a caliper is used to measure the length and  
279 diameter, and calculate the sample bulk volume. For this study, the calculation of the  
280 porosities using the three different instruments have been made using a single bulk

281 volume for each sample in order to minimize potential discrepancies that could arise from  
282 three different manual caliper measurements.

283 A total of 30 samples were thus sent to AGAT Laboratories. Prior to analyses, samples  
284 are dried in a convection oven for 48 h at 108°C. The helium pressure is set at 2.76 MPa.  
285 Porosity values were given a margin of error of +/- 0.005 (0.5 %). Hereafter this  
286 equipment will be referred as in-house AGAT gas porosimeter (IHAP).

287 A total of 20 porosity measurements were made using the Core Test Systems AP-608 Gas  
288 permeameter-porosimeter available at INRS “Laboratoire ouvert de géothermie” (LOG;  
289 Québec, Canada). Prior to analyses, samples were first dried at 108°C for at least 48 h,  
290 using a Thermolyne oven (Thermo Scientific). Initial helium pressure is set at 1.38 MPa.  
291 In order to examine the reliability of analysis results, each core plug was analysed three  
292 times and the results were averaged. This procedure delivered porosity results with an  
293 average standard deviation of 0.18. Only 20 reference samples were analysed because of  
294 diameter and length restrictions associated with the AP-608 instrument (Tab. 1-2).

295 Few samples were also analysed at the INRS laboratory for Decontamination and Waste  
296 Reclamation, using a gas pycnometer (Micromeritics AccuPyc 1330). Routinely used to  
297 obtain the density, the device uses the Boyle’s Law to measure grain volumes. The  
298 instrument is fully-automatic and makes three consecutive runs for each analysis. Only 10  
299 reference samples were analysed because of diameter and length restrictions associated  
300 with this instrument (Tab. 1-2).

301 3-2 Silurian core samples

302 Silurian core samples with their 1 7/8 inch (47.625 mm) diameter could only be analysed  
303 by the IHAP at AGAT Laboratories. Out of the 18 cores from the hydrothermal dolomite  
304 interval (Fig. 4), five samples were sent to AGAT Laboratories, after the core-flooding  
305 experiment was completed. These five samples were chosen to represent the natural  
306 heterogeneity of the interval. A detailed description of all five sample is given (Figure  
307 4B).

308 3) Core-flooding experiment

309 4-1 System

310 An in-house core-flooding system was designed to accommodate different sample sizes  
311 (diameter and length) and to control experimental variables. The system was built to be  
312 simple, reliable and cost effective (Fig. 5). One (or several) horizontal chamber, made of  
313 polyvinyl chloride (PVC) or acrylic (plexiglass), an X-ray-transparent material, is  
314 connected to two pumps and a water tank. The core holder inside diameter is 41.7mm and  
315 50.8mm for 1<sup>1/2</sup>" and 1<sup>7/8</sup>" samples, respectively. Between chambers, Swagelok quick  
316 connects (valves) are used because they allow minimal air inclusion and minimal  
317 spillage. The laboratory vacuum pump (Welch, WOB-L Pump 2585) is used to adjust and  
318 monitor the vacuum level. A diaphragm pump (SHURflo, 2088 serie) is used to ensure  
319 constant fluid circulation through the chamber at a flow rate 19.28 l/min. Within the  
320 chamber, the internal fittings use customized 3D printed PLA (polylactic acid) core  
321 holders to increase stability and create space for water flow around the samples,  
322 particularly when the chamber is flooded. For the purpose of this work, core-flooding was  
323 performed either with distilled water or sodium iodide solution. All reference samples

324 (n= 30) were saturated using distilled water. In addition, 15 samples (see Tab.4) were  
325 saturated using sodium iodide salt (NaI). NaI was chosen because its behaviour is similar  
326 to NaCl with respect to argillaceous minerals (Withjack, 1988). In addition, it has a  
327 reasonable cost, approximately 170\$ per 100g, and can be handle safely without causing  
328 hazards.

#### 329 4-1 Protocol

330 Core-flooding experiments were conducted at room temperature and no confinement  
331 pressure was applied (workflow is summarized in Fig. 6). Prior to scanning, samples  
332 were dried at 108°C for at least 48 h, using a Thermolyne oven (Thermo Scientific). In  
333 agreement with Ketcham and Iturrino (2005) , a two-stage scanning protocol was used.  
334 Samples were placed in the sealed chamber and first scanned in a dry state. Secondly,  
335 vacuum is applied for 24hours, degassing distilled water and samples simultaneously.  
336 Then the chamber is flooded with either water or NaI solution (15 g/L), during which the  
337 diaphragm pump guarantees constant fluid circulation. This removes air bubbles that  
338 could be created during the saturation process, thus maximising fluid contact and  
339 reducing the number of connected pores that would not be saturated otherwise. It also  
340 constantly provides degassed water at sample-water interface thus extracting residual air  
341 bubbles. The use of NaI doping agent, with a concentration of 15 g/L, increases contrast  
342 by 30% when compared to water. Such improvement can be crucial when investigating  
343 small pore size that falls below the range of medical CT resolution. Core samples were  
344 weighted before and after saturation with either water or NaI to evaluate the performance  
345 of the saturation process. Sample weight was measured with a Sartorius top-loading  
346 balance (CP4202S) having a 0.01 g accuracy. According to the Liquid saturation

347 technique (API, 1998), pore volume can be calculated using bulk volume and known  
348 fluid density (water and NaI).

#### 349 4) CT-scan measurements

350 CT measurements were performed using a Siemens SOMATOM Definition AS+ 128 at  
351 INRS-ETE. The X-ray tube of the CT scanner was operated at a voltage of 140 kV and a  
352 current of either 700 or 350 mAs for reference samples and core samples of the study  
353 area, respectively. The same voltage for all CT acquisition was used in order to obtain  
354 comparable HU values. However, the current had to be adapted to minimize downtime  
355 due to X-ray source cooling. Longer core holder, such as the one used for the Silurian  
356 carbonate interval, allowed more samples to be processed simultaneously. The source  
357 current was then reduced from 700 mA to 350mA, thus using less power and generating  
358 less heat. Downtime between scans, using high X-ray source power, can be more than 15  
359 minutes, adding hours of waiting time thus increasing significantly the operating cost. An  
360 H70h convolution kernel was used for the reconstruction of the images. The thickness of  
361 each CT slice was set to 0.6 mm (Tab. 3). Images were recorded in DICOM format and  
362 visualizes with the open-source software Fiji (Schindelin et al., 2012).

#### 363 5) Noise reduction

364 Density changes associated with the infiltration of water can be subtle when porosity is  
365 low. In such cases, image noise is problematic and could outweigh the density variation  
366 associated with the water saturation. The Pini and Madonna (2016) approach was  
367 therefore adopted here to examine how the level of noise changed when averaging several  
368 scans or decreasing the resolution, and how this ultimately affected the porosity

369 calculation (Fig. 7). The scan repetition for this study was set to three in order to get a  
370 short acquisition time with a low image noise from this method.

#### 371 6) Beam hardening

372 The beam hardening is a common artefact caused by the absorption of low energy photon  
373 at sample frontier thus “hardening” the beam by making the mean energy higher. This  
374 phenomena, linked with the polychromatic nature of the X-ray spectra emitted, produce  
375 density under-estimation at sample center (Ketcham and Carlson, 2001). A software  
376 beam-hardening correction to detector readings is applied by the scanner and is optimized  
377 for human body, which mainly consist of water. This correction does not remove the  
378 artefact due to rock samples. Ketcham and Itturino (2005) have showed that the sample  
379 geometry changes the beam hardening profile thus a calibration wedge with a similar  
380 density and diameter is required. The strategy to minimize the beam hardening profile  
381 variation from dry to saturated was to build a core holder with an internal diameter close  
382 to the sample diameter. This creates a nearly identical geometry between dry and  
383 saturated state, thus producing a near equivalent beam hardening profile. Moreover, the  
384 image subtraction applied at the next stage minimizes the influence of beam hardening.

#### 385 7) Data analysis

386 Data analysis is based on the X-ray saturation technique (Withjack, 1988) but also  
387 includes recent developments (Ketcham and Iturrino, 2005; Pini et al., 2012; Pini and  
388 Madonna, 2016). Algorithms applied aim at determining porosity by comparing CT  
389 images in a saturated state and unsaturated state. The working hypothesis considers a  
390 voxel as a mixel that is a mixture of porosity and solid phase material. Density value of  
391 one mixel is therefore an average value of its content. When saturating the samples with

392 water or NaI, the connected pores, initially filled with air, is filled with the liquid phase.  
393 Since solid phase density and quantity do not change, recorded changes in voxels density  
394 are interpreted as the results of pore filling. Equations below (1) summarize the  
395 calculation of porosity from density matrices acquired (D).

$$396 \quad \%porosity = \frac{D_{dry} - D_{saturated}}{D_{gas} - D_{fluid}} \quad (1)$$

397 The calculation is applied for each voxel containing the sample. Grain density is not  
398 needed to evaluate porosity since only fluid density in pores changes (Boespflug et al.,  
399 1994). Fluid density is known as part of CT calibration ( $D_{gas} = D_{air} = -1000$  HU;  $D_{fluid} =$   
400  $D_{water} = 0$  HU), while the density of the NaI solution in Hounsfield unit was obtained by  
401 in situ calibration ( $D_{NaI} = 324$  HU, for a 15g/L NaI solution).

402 The subtraction of the saturated vs dry data to calculate the porosity was performed using  
403 MATLAB®. Prior to subtraction, data registration was performed for each analysis using  
404 intensity-based image registration algorithm (MathWorks, 2018). The 3D matrix resulting  
405 of this subtraction allowed to visualize the effective pore network and the evaluation of  
406 the porosity distribution using statistics. In some instance, a circular binary mask has  
407 been used to include large vugs located at sample surface. The algorithm uses Hough  
408 transform and phase-coding (Yuen et al., 1990).

## 409 **RESULTS**

410 The results obtained in this study are divided into three main sections. The two first  
411 sections correspond to porosity measurements made on the reference samples set only  
412 ( $n = 30$ ), either using the different helium gas porosimeters (i.e AccuPyc, AP-608 and  
413 IHAP); or using the improved medical CT-scan methodology (Tab. 4). The third section

414 presents the results obtained for the silurian core samples, using both IHAP and the  
415 improved medical CT-scanning methodology (Tab. 5).

416 In addition to exact porosity values obtained from different instruments (AP-608,  
417 AccuPyc, IHAP or CT-scan), several correlation ratios are then considered in these  
418 results sections. Firstly, because the helium porosity measurements made using the IHAP  
419 are considered as true values, the notion of absolute error is calculated with respect to the  
420 helium porosity (Table 4-5). Second, the absolute error (AE) corresponding to the amount  
421 of error in the porosity measurements is calculated, i.e. from the difference between the  
422 porosity calculated using the improved CT-scan methodology and the porosity measured  
423 using a conventional gas porosimeter. The R-squared ( $R^2$ ), commonly used in classical  
424 regression analysis (Rao et al., 1973), is calculated and represents a statistical measure of  
425 how close the data are to the fitted regression line. Also known as the coefficient of  
426 determination,  $R^2$  ranges from 0 to 1. In the present work,  $R^2$  is calculated to compare two  
427 instruments or methodology evaluating the porosity. Finally, the root-mean-square error  
428 (RMSE) is calculated. It corresponds to the standard deviation of the residuals (prediction  
429 errors). Residuals are a measure of how far from the regression line data points are.  
430 RMSE therefore represents how concentrated the data is around the line of best fit.  
431 Applied to this paper, the line of best fit would correspond to a perfect match between  
432 porosity measured with the CT-scan and that measured by AGAT laboratories using a  
433 conventional helium gas porosimetry. RMSE was used to give an idea of how well the  
434 CT-scan porosity matches the gas porosity obtained conventionally.

## 435 1) Helium porosity

436 The results allow for comparison of gas porosity obtained from three distinct instruments  
437 and laboratories (Tab. 2; 4; Fig. 8A-C). All three methods are simple and rapid  
438 techniques widely used to measure porosity on core samples. The porosity obtained from  
439 Boyle's law gas porosimeters (Fig. 8A and B), IHAP, AP-608 and AccuPyc, shows linear  
440 relationships with a  $R^2$  coefficient ranging from 0.98 to 0.99 and a slope close to 1 (from  
441 0.97 to 1.03). Accupyc and AP-608, with both measurement made at INRS, show the  
442 smallest RMSE (0.43%) when compared with IHAP (0.8% for Accupyc and 0.94% for  
443 AP-608). The larger differences between AP-608 and Accupyc (Fig. 8C) occur for  
444 limestone samples (Indiana and Carthage) that are known to be genetically more complex  
445 and spatially heterogeneous rocks (Galaup et al., 2012; Freire-Gormaly et al., 2015).  
446 Therefore, differences in porosity evaluation were expected. The same trend is observed  
447 when comparing IHAP with Accupyc and AP-608. This specific carbonate sample has a  
448 highly irregular surface (Fig. 9), with visible vugs and dissolved bioclasts on the exterior  
449 surface. Rock texture at surface can affect basic physical measurements such as length,  
450 particularly those made with a caliper, and in turn, can induce uncertainty in porosity  
451 estimation. Based on these comparison, results from sandstone samples appears to be  
452 more consistent. Analysis obtained from AGAT Laboratories were chosen as the most  
453 reliable since this private and independent laboratory runs routine petrophysical  
454 properties analyses (including helium gas porosimetry) for the private oil and gas sector  
455 as well as for academic and governmental research.

## 456 2) CT-scan porosity - reference samples

457 CT-scan porosity results are compared to IHAP only as the later values were validated  
458 using the two different instruments and can therefore be considered as a reference (Fig.  
459 10). The porosity obtained by the IHAP and CT-scan method ( $n=30$ ) shows a linear  
460 relationships with a  $R^2$  coefficient of 0.99 and a slope close to 1 (0.91). When comparing  
461 CT-scan-IHAP with AP-608-IHAP, RMSE is more than two times higher (Fig. 8A). This  
462 difference is significant and tends to increase as porosity increases (Fig. 10). That can be  
463 explained by the fact that more porosity means more water present inside the sample thus  
464 a stronger beam hardening artefact variation. It leads to a larger underestimation of the  
465 porosity as beam hardening creates a greater underestimation of the density in the  
466 saturated state data.

467 A correction factor ( $1/0.91$ ) was calculated using linear regression to minimize that  
468 difference (Fig. 10). This correction brings the RMSE down to 0.54% (Fig. 11), which is  
469 lower than AP-608 versus IHAP RMSE value (Fig. 8A), but slightly higher than AccuPyc  
470 versus AP-608 RMSE (Fig. 8C). This correction factor was applied to all data points and  
471 for all subsequent analyses. As already experienced by Ketcham and Iturrino (2005) ,  
472 some voxels have estimated porosity values below 0 % (and above 100 %), due to image  
473 noise and possible remaining misfit between data sets.

474 When considering each lithology type (Fig. 12), the CT-scan method seems to be less  
475 robust with dolomite rock samples, where  $R^2$  decreases down to 0.83 (Fig. 12C) and  
476 RMSE is slightly higher. More data points would be needed to fully analyze these  
477 relationships. The influence of porosity range has then been considered (Fig. 13) and  
478 porosities values obtained using medical CT appears to be equally valid for the entire

479 range of porosities tested (from 1.5 to 34%), with  $R^2$  around 0.98 (Fig. 13) and RMSE  
480 close to 0.5. The possible influence of core diameter was also investigated.

481 When comparing porosity results of 1<sup>1/2</sup>" and 1<sup>7/8</sup>" core diameter (Fig. 14),  $R^2$  are very  
482 similar, with 0.99 (Fig. 14A) and 0.98 (Fig. 14B) respectively. However, RMSE increases  
483 from 0.43 to 0.72 %, from small to large diameter which seems to indicate that, even after  
484 linear correction, CT-scan method seems to produce more reliable porosity estimation for  
485 smaller diameter samples.

486 Lastly, CT-scan porosity results using doping agent are also compared with IHAP (Fig.  
487 15) and show a linear relationship with a  $R^2$  coefficient of 0.99 and RMSE equals to  
488 0.70%. These results are comparable to those obtained with water saturation and the  
489 benefits of using NaI seems less important than initially expected.

### 490 3) CT-scan porosity – Silurian core interval

491 The selected HTD core interval (Fig. 4A) was subsampled and a 1.8 m continuous section  
492 was scanned using the core-flooding setup. The interval actually corresponds to 18 core  
493 subsamples (see Fig. 4 and Fig. 16). Within this 1.8 m interval, five isolated samples  
494 were also sent to AGAT laboratories to validate locally the CT-scan porosity values (Fig.  
495 4B; namely CSI-2, 3, 10, 12 and 16). Small gaps between core sub-samples were taken  
496 into consideration and depths were corrected to account for these gaps. Different  
497 statistical profiles describing porosity were generated (Fig. 16) with a spatial resolution of  
498 0.6 mm. Mean porosity profile and heterogeneity profile indicate that porosity is lower in  
499 the upper part of the depth interval but more heterogeneous, with a rather sharp transition  
500 between subsamples CSI-7 and CSI-8 (Fig. 16). Another interesting observation is the

501 occurrence of increased porosity intervals (with values higher than 10%) that seems to be  
502 limited to 10-15 cm thick interval (see for example within CSI-12 or 18). Such  
503 information would be completely missed if considering discrete samples only for helium  
504 gas porosity measurements. In addition to provide an average porosity value, CT-scan  
505 porosity dataset also provides valuable spatial information about the porosity within  
506 samples and allows porosity visualization in 3D (Fig. 17). Looking at diverse 3D views  
507 from each sample individually, qualitative information is added, such as porosity  
508 distribution vertically and horizontally, at the centimetric scale. For instance, within  
509 sample CSI-2, largest macropores are homogeneously distributed within the sample and  
510 correspond to isolated vugs (Fig. 17A), whereas in sample CSI-5, largest macropores are  
511 limited to specific areas of the sample, associated to oblique fractures (Fig. 17B).

## 512 **DISCUSSION**

### 513 1) Porosity interpretation

#### 514 Reference samples

515 Overall porosity correlation is a bit better for sandstone samples (Fig. 12). However,  
516 RMSE for all lithologies remain quite close (and all  $<0.7\%$ ). RMSE increases slightly  
517 from SST to LST and then Dol, a trend that coincide with porosity data points grouped  
518 more tightly (around 10% porosity approximately). The number of samples changes from  
519  $N=14$  to  $N=6$ , which can further affect the RMSE estimation. Even though our study use  
520 a large number of samples ( $n=32$ ) compared to the available literature, it is obvious that  
521 the number of samples influences the quality of the results in a statistical point of view. In  
522 future works, we plan to extend porosity range for limestone and dolomite to have truly  
523 comparable dataset. However, the better porosity correlation for sandstone could very be

524 statistically valid and genetic in nature, and this well-known in the literature (Lucia,  
525 2007; Bust et al., 2011; Victor et al., 2017). Carbonates and dolomites, because of their  
526 chemical reactivity have more complex diagenetic history and hence porosity  
527 distribution. Because of their physical properties and generally lower chemical reactivity,  
528 clastic sediments have more homogeneous porosity distribution to the contrary of  
529 carbonates in which heterogeneous distribution of calcitic, aragonitic and dolomitic  
530 components (particle, cement) will lead to irregular distribution of reactive particles to a  
531 specific fluid, and hence variable, even erratic, porosity development at the very fine  
532 scale.

533 Silurian core interval

534 The porosity evaluation of the Silurian core interval using CT-Scan (Fig. 16) gives  
535 clearly heterogeneous values as expected given the nature of samples. The core  
536 encompasses a mix of lithologies that do not appear affected by fracture-controlled  
537 hydrothermal fluid circulation (Fig. 3A) and intervals with diverse degrees of  
538 hydrothermal alteration (see Fig. 3B). The whole core set is a mix of preserved  
539 depositional limestone facies (non-porous low energy depositional environment  
540 represented by lime mudstone and wave reworked porous bioclastic limestone) and  
541 hydrothermally altered diagenetic facies.

542 The improved methodology using medical CT-scan allows mapping out the porosity at a  
543 centimetric scale, something impossible to achieve through conventional approaches. The  
544 added value of the improved methodology is well illustrated when comparing dry state  
545 CT-scan images of two dolomitic samples with similar porosity value (around 9.5 %; Fig.

546 18; Table 4-5). A reference sample (SI-K-15A) presents circular to ovoid mesopores  
547 mainly concentrated on the lower half of the specimen (Fig. 18A). Macro/mesopores  
548 appear disconnected from one another, at least at the medical-CT scale resolution. The  
549 core sample coming from the silurian hydrothermally altered interval is completely  
550 different (Fig. 18B), even though core-averaged porosity value are very close.  
551 Macropores are much larger and their distribution is highly heterogeneous. Such  
552 qualitative information cannot be deduced from conventional helium porosity. In  
553 addition, when these two samples are analysed by our improved methodology, core-  
554 averaged porosity values are different. The reference samples, Si-K-15A, has a lower  
555 porosity estimates (8.31%) whereas the silurian sample hydrothermally altered has a  
556 higher porosity estimates (11.3%). Looking at the images (Fig. 18), the CT-scan, core-  
557 averaged, porosity values appears to be more realistic.

## 558 2) Advantages of this new CT scan methodology

559 The average CT porosity value for each reference sample has been used to validate the  
560 methodology but the ultimate goal is to access the spatial distribution of porosity and acquire  
561 further information on porosity at the macro scale. To achieve that, 2D and 3D visualisation  
562 can be performed on the dataset to qualitatively describe the porosity distribution.  
563 Quantitative statistics can also be derived to better describe not only porosity values but also  
564 its spatial distribution: pore concentration at specific levels, heterogeneity variation with  
565 function of depth, etc.

566 The experimental setup developed in the present study is cost-effective and easy to handle  
567 (Fig. 5), especially when compare to previous core-flooding experiments found in the  
568 literature (Hove et al., 1987; Vinegar and Wellington, 1987; Withjack, 1988), often using

569 costly pressure vessels made of aluminium chamber and Teflon casing (i.e. Hassler type core  
570 holder; (Karacan et al., 2003). Different from Ketcham and Iturrino (2005) , our current setup  
571 presents no risk of fluid loss while saturation and scanning phases because samples stay  
572 within the core holder at all times. Numerical realignment of dry and wet states allows to  
573 perform samples saturation phase (a minimum of 72 hours duration) outside of the CT  
574 scanner requiring the use of the CT facility for a very limited amount of time. The low costs  
575 of the core holder (PVC or Plexiglas) and custom, 3D printed internal fittings (PLA), makes  
576 it easy to design a decimetric core-holder and analyse several samples at the same time. As a  
577 matter of fact, the cost-effectiveness of both setup and protocol allowed to perform CT-scan  
578 based porosities determination on 30 isolated samples and a 1.6 m thick core section. This is,  
579 to the best of our knowledge, the first attempt ever made to run core-flooding experiments  
580 under CT on such a large number samples (Tab. 1; Fig. 1). The scan time is quite reasonable  
581 (2 minutes for 3 repeated scan on a 10cm sample), data processing time is fast (6 minutes)  
582 and the method is scalable to process tens of meters of core samples. The saturation process  
583 was performed for a week as the maximum water saturation was desired but this process  
584 could be optimized by adjusting the following variables: (1) degassing time, (2) vacuum and  
585 water circulation time and (3) water circulation duration without vacuum (Fig. 6). The second  
586 step takes most of the process time and might be reduced considering the porosity level of the  
587 sample. It might also be desirable to spend more time on the step 3 as remaining air bubbles  
588 shrink in size and thus allow more water in. Likewise, it might be more effective to perform  
589 alternative vacuum during step 2, as this could split entrapped air into smaller bubbles which  
590 could then be extracted from the sample.

591 Different approaches used to derive quantitative information from CT data needs calibration.  
592 Converting HU to density profiles requires subsampling, volume and weight measurements

593 (Boespflug et al., 1994; Amos et al., 1996; ASTM-E1441-11, 2011). Mineralogy and porosity  
594 variation obtained from “CT dual energy” acquisition are results derived from effective  
595 atomic number and density profiles, which in turn needs calibration from materials standards  
596 to convert X-ray absorption measurement (Van Geet and Swennen, 2001; Walls and  
597 Armbruster, 2012; Lopez et al., 2016). Calibration is a non-trivial process and cumulates  
598 errors from each additional required measurement. The proposed approach includes  
599 calibration, as it requires air and fluid HU values, but is straightforward and taken in situ, for  
600 every measurement made. Air HU value is measured while scanning samples at dry state and  
601 fluid HU value during the saturated state scans.

602 No prior knowledge about mineralogy, density or porosity range is needed with the present  
603 methodology to obtain a reliable porosity value (Figs. 10-16; Table 4-5). CT-scan porosities  
604 obtained for dolomite samples are little less correlated with porosities values obtained by  
605 conventional porosimetry, but overall lithology type still has a low influence on results (Fig.  
606 12).

607 One of the main difference between porosities derived from CT-scan versus those given by  
608 gas porosimeter is its independence from volume calculation. Gas porosimeters measure  
609 grain volume. The porosity is then calculated using bulk volume of sample which is based on  
610 linear measurements of samples with a caliper and the application of the appropriate  
611 geometric formula. Therefore, this method is subject to human error and measurement error if  
612 the sample is irregularly shaped (e.g. Fig. 9).

613 Lastly, working at medical CT scale represents an advantage when considering scanning time  
614 and sample size. With our working parameters (Tab. 3), acquisition time is few seconds to  
615 minutes, compare to micro or nano-CT where total data acquisition times span from hours to

616 ten of hours (Cnudde and Boone, 2013; Bultreys et al., 2016a) and where sample size is often  
617 limited to only few millimeters (Pini and Madonna, 2016), which brings back the question of  
618 the representativeness.

### 619 3) Limitations

620 One limitation of the proposed approach is the need to further correct beam hardening effects.  
621 The original postulate was that artefacts such as beam hardening do not need to be corrected  
622 because (1) the geometry is cylindrical (Pini and Madonna, 2016) and (2) remains constant  
623 through flooding experiment, i.e. beam hardening effect would be canceled out via the  
624 subtraction of wet and dry datasets. However our results have shown that the difference  
625 increases linearly as the porosity increases (Fig. 8). More porous samples (therefore  
626 associated with the greatest difference between the two states), are associated with lower  
627 correlations with gas-measured porosity values. Nonetheless, our current dataset suggests that  
628 a simple linear correction seems to account well for the residual influence of beam hardening  
629 (Fig. 10-11).

630 Cylindrical samples ease the selection of a versatile and low cost core holder material that  
631 would then accommodate a large range of sample diameter. However the restrictive  
632 geometry itself could be seen as a limiting factor. Without proper and full beam  
633 hardening correction, the analysis of randomly shape rock fragments and other sample  
634 geometry remains difficult under CT-scan. At best, qualitative information could be  
635 obtained from non-cylindrical specimen.

### 636 4) Perspectives on future work (s)

637 Future research efforts should explore whether the experimental protocol, the acquisition  
638 parameters or the data analysis itself can be optimized by lithology type or porosity

639 range. Maybe one or two repeated scans would be enough and therefore could lower the  
640 cost to some instances.

641 Another key point for further works is to test upscaling possibilities. In particular, the  
642 calibration of wireline logs profiles using the CT-scan porosity profiles, instead of  
643 discrete porosity values from plugs, is promising. CT-scan images can be correlated  
644 directly with density well log because they both measure the amount of Compton  
645 scattering, proportional to bulk density (Wellington and Vinegar, 1987). With the high  
646 levels of heterogeneity inherent in carbonate reservoirs, correlation between low  
647 resolution e-logs and high resolution, discrete, poro-perm measurements has been  
648 debated (Delhomme et al., 1996; Tilke et al., 2006). The medical CT and its range of  
649 investigation could well bridges the gap.

650 As already stated, the production of 3D porosity matrix images (e.g. Fig. 17) opens the  
651 opportunity to produce 3D models and run numerical flow simulations, at the centimetric  
652 or tens of centimeter scale. This would be of interest for many research fields such as oil,  
653 gas and geothermal reservoirs, hydrogeology or CO<sub>2</sub> sequestration.

654 CT-scan images were only made at the initial (samples filled with air) and final stages  
655 (samples filled with distilled water), therefore no information regarding transitional  
656 saturation conditions, wetting characteristics of rocks or permeability were gained.  
657 Compared to similar studies in this field of research (Vinegar and Wellington, 1987;  
658 Wellington and Vinegar, 1987; Withjack, 1988), there is no gas/fluid front to track.  
659 Furthermore, the current setup rely only on capillary forces to saturate the rock samples.  
660 Said differently, no fluid forcing is applied. One can argue that porosity data alone are

661 insufficient. Two samples with similar porosity values can have significantly different  
662 permeability. However, the current setup not only allows the assessment of an average  
663 porosity value per sample, but also provides a 3D porosity matrix (Fig. 17). This in turn,  
664 can be transformed into 3D models and used to run numerical flow simulations using  
665 commercial software such as COMSOL. Such approach has already been tested with  
666 micro-CT and medical CT measurements (e.g. Zaretskiy et al., 2010; Bultreys et al.,  
667 2015). To our knowledge, this has not commonly been achieved on heterogeneous  
668 carbonate samples, for which pore structure measurements are mostly based on mercury  
669 injection (Galaup et al., 2012), eventually combined with micro-CT for low porosity  
670 carbonate (Fusi and Martinez-Martinez, 2013). A lot of work has been done in terms of  
671 fluid flow modelling and simulation (see Review papers by Meakin and Tartakovsky  
672 (2009) ; Blunt et al. (2013) and references therein) and might be adapted to our (medical)  
673 CT-scan porosity dataset.

#### 674 **CONCLUSION**

675 This work developed an effective and practical method using medical-CT to reliably  
676 estimate reservoir porosity for spatially heterogeneous material such as fractured or  
677 dolomitized carbonates, incorporating recent advances in data correction.

678 (1) The in-house core-flooding setup is low cost, simple, and easy to operate. Several  
679 individual core samples can be scanned simultaneously (dry and saturated), as well as  
680 continuous core sections up to 1.5 m long. Scanning a sample in a dry state and saturated  
681 state, performing a three-dimensional alignment and subtracting the two data sets allow  
682 the construction of 3D porosity matrices.

683 (2) Based on a set of reference core material, this study illustrates the relationship  
684 between porosity assessed by CT-scan against the ones obtained by conventional gas  
685 porosimetry techniques. A strong correlation is observed between both techniques so that  
686 the current CT-scan methodology appears to be a reliable and accurate way to estimate  
687 fine-scale variations of porosity for the main types of sedimentary rocks, in a wide range  
688 of porosity value.

689 (3) This consistency opens up the possibility to extend porosity assessment beyond gas  
690 porosimetry, particularly for heterogeneous carbonate samples. The added value of the  
691 porosity measurement by CT-scan is the generation of 3D images of pore network,  
692 allowing to assess spatial attributes of macropores, their distribution and connectivity.

693 (4) Last, but not least, the CT-scan method allows the construction of continuous porosity  
694 profiles that are well correlated with discrete helium gas porosity values.  
695 Millimetric/centimetric scale data are rarely available in subsurface datasets and reliable  
696 continuous porosity measurement at this scale is a step forward in the understanding of  
697 reservoir properties.

#### 698 **ACKNOWLEDGMENTS**

699 The authors would like to thank *Ressources et Énergie Solutex Inc.* for financial support  
700 and for giving access to samples, as well as for permission to publish this paper. The  
701 project was mainly supported by the Natural Sciences and Engineering Research Council  
702 of Canada (NSERC) through Engage Grants (EGP-491145-15 and EGP2-510269-17).  
703 The first author was supported by a Mitacs Acceleration postdoctoral Grant (IT 06251)  
704 and subsequently by a postdoctoral fellowship of the Geological Survey of Canada with

705 operational funds from the Environmental Geoscience Program of the Land and Mineral

706 Sector of Natural Resources Canada.

707

ACCEPTED MANUSCRIPT

708 **REFERENCES**

- 709 Akin, S. and A. Kovscek (2003). "Computed tomography in petroleum engineering  
710 research." Geological Society, London, Special Publications 215(1): 23-38.
- 711 Alemu, B. L., E. Aker, M. Soldal, Ø. Johnsen and P. Aagaard (2013). "Effect of sub-  
712 core scale heterogeneities on acoustic and electrical properties of a reservoir rock: a CO<sub>2</sub>  
713 flooding experiment of brine saturated sandstone in a computed tomography scanner."  
714 Geophysical Prospecting 61(1): 235-250.
- 715 Alves, H., I. Lima and R. T. Lopes (2014). "Methodology for attainment of density and  
716 effective atomic number through dual energy technique using microtomographic images."  
717 Applied Radiation and Isotopes 89: 6-12.
- 718 Amos, C., T. Sutherland, B. Radzjewski and M. Doucette (1996). "A rapid technique to  
719 determine bulk density of fine-grained sediments by X-ray computed tomography."  
720 Journal of Sedimentary Research 66(5).
- 721 Anderson, S., H. Wang, R. Peyton and C. Gantzer (2003). "Estimation of porosity and  
722 hydraulic conductivity from X-ray CT-measured solute breakthrough." Geological  
723 Society, London, Special Publications 215(1): 135-149.
- 724  
725 Andrianov, A., R. Farajzadeh, M. Mahmoodi Nick, M. Talanana and P. L. Zitha (2012).  
726 "Immiscible foam for enhancing oil recovery: bulk and porous media experiments."  
727 Industrial & Engineering Chemistry Research 51(5): 2214-2226.
- 728  
729 API (1998). RP40, Recommended practices for core analysis, 2nd Ed. Washington, DC,  
730 American Petroleum Institute.
- 731  
732 ASTM-E1441-11 (2011). Standard Guide for Computed Tomography (CT) Imaging.  
733 ASTM International, West Conshohocken, PA, DOI: 10.1520/E1441-11
- 734  
735  
736 Baniak, G. M., M. K. Gingras and S. G. Pemberton (2013). "Reservoir characterization of  
737 burrow-associated dolomites in the Upper Devonian Wabamun Group, Pine Creek gas  
738 field, central Alberta, Canada." Marine and Petroleum Geology 48: 275-292.
- 739  
740 Biswal, B., R. J. Held, V. Khanna, J. Wang and R. Hilfer (2009). "Towards precise  
741 prediction of transport properties from synthetic computer tomography of reconstructed  
742 porous media." Physical Review E 80(4): 041301.
- 743  
744 Black, M. E. (2014). "Porosity and permeability in the Graminia Formation, Upper  
745 Devonian Winterburn Group in the Germain Field, northeastern Alberta."

- 746  
747 Blunt, M. J., B. Bijeljic, H. Dong, O. Gharbi, S. Iglauer, P. Mostaghimi, A. Paluszny and  
748 C. Pentland (2013). "Pore-scale imaging and modelling." *Advances in Water Resources*  
749 51: 197-216.
- 750  
751 Boespflug, X., N. Ross, B. Long and J. Dumais (1994). "Tomodensitométrie axiale:  
752 relation entre l'intensité tomographique et la densité de la matière." *Canadian Journal of*  
753 *Earth Sciences* 31(2): 426-434.
- 754  
755 Boon, M., B. Bijeljic and S. Krevor (2017). "Observations of the impact of rock  
756 heterogeneity on solute spreading and mixing." *Water Resources Research* 53(6): 4624-  
757 4642.
- 758  
759 Bose, C. C., B. Alshatti, L. Swartz, A. Gupta and R. Barati (2014). Dual application of  
760 polyelectrolyte complex nanoparticles as enzyme breaker carriers and fluid loss additives  
761 for fracturing fluids. *SPE/CSUR Unconventional Resources Conference–Canada*, Society  
762 of Petroleum Engineers.
- 763  
764 Bourque, P., D. Brisebois and M. Malo (1995). "Gaspé belt." *Geology of the*  
765 *Appalachian–Caledonian Orogen in Canada and Greenland*. Edited by H. Williams.  
766 *Geological Survey of Canada, Geology of Canada*(6): 316-351.
- 767  
768 Bultreys, T., M. A. Boone, M. N. Boone, T. De Schryver, B. Masschaele, L. Van  
769 Hoorebeke and V. Cnudde (2016a). "Fast laboratory-based micro-computed tomography  
770 for pore-scale research: Illustrative experiments and perspectives on the future."  
771 *Advances in Water Resources* 95: 341-351.
- 772  
773 Bultreys, T., W. De Boever and V. Cnudde (2016b). "Imaging and image-based fluid  
774 transport modeling at the pore scale in geological materials: A practical introduction to  
775 the current state-of-the-art." *Earth-Science Reviews* 155: 93-128.
- 776  
777 Bultreys, T., L. Van Hoorebeke and V. Cnudde (2015). "Multi-scale, micro-computed  
778 tomography-based pore network models to simulate drainage in heterogeneous rocks."  
779 *Advances in Water Resources* 78: 36-49.
- 780  
781 Bust, V. K., J. U. Oletu and P. F. Worthington (2011). "The challenges for carbonate  
782 petrophysics in petroleum resource estimation." *SPE Reservoir Evaluation & Engineering*  
783 14(01): 25-34.
- 784

- 785 Caliskan, S. and A. Shebatalhamd (2017). Examining Heterogeneity Based on the  
786 Computerized Tomography Imaging. SPE Kingdom of Saudi Arabia Annual Technical  
787 Symposium and Exhibition, Society of Petroleum Engineers.
- 788
- 789 Chadwick, R. A., P. Zweigel, U. Gregersen, G. A. Kirby, S. Holloway and P. N.  
790 Johannessen (2004). "Geological reservoir characterization of a CO<sub>2</sub> storage site: The  
791 Utsira Sand, Sleipner, northern North Sea." *Energy* 29(9): 1371-1381.
- 792
- 793 Churcher, P., P. French, J. Shaw and L. Schramm (1991). Rock properties of Berea  
794 sandstone, Baker dolomite, and Indiana limestone. SPE International Symposium on  
795 Oilfield Chemistry, Society of Petroleum Engineers.
- 796
- 797 Cnudde, V. and M. N. Boone (2013). "High-resolution X-ray computed tomography in  
798 geosciences: A review of the current technology and applications." *Earth-Science*  
799 *Reviews* 123: 1-17.
- 800
- 801 Coles, M., E. Muegge and E. Sprunt (1991). "Applications of CAT scanning for oil and  
802 gas production." *IEEE Transactions on nuclear science* 38(2): 510-515.
- 803
- 804 Connell-Madore, S. and T. Katsube (2007). Pore-size distribution of samples from the  
805 Mallik 5L-38 well, Northwest Territories, Geological Survey of Canada.
- 806
- 807 Davis, L. A., R. M. Moss and G. P. Pepin (1992). "Direct measurement of the constituent  
808 porosities in a dual-porosity matrix." *The Log Analyst* 33(02).
- 809
- 810 Delhomme, J. P., J. Bedford, N. M. Colley and M. C. Kennedy (1996). Permeability and  
811 Porosity Upscaling in the Near-Wellbore Domain: The Contribution of Borehole  
812 Electrical Images. European Petroleum Conference. Milan, Italy, Society of Petroleum  
813 Engineers: 13.
- 814
- 815 Denney, D. (2004). "Digital core laboratory: reservoir-core properties derived from 3D  
816 images." *Journal of Petroleum Technology* 56(05): 66-68.
- 817
- 818 Devarapalli, R. S., A. Islam, T. F. Faisal, M. Sassi and M. Jouiad (2017). "Micro-CT and  
819 FIB-SEM imaging and pore structure characterization of dolomite rock at multiple  
820 scales." *Arabian Journal of Geosciences* 10(16): 361.
- 821
- 822 Dietrich, J., D. Lavoie, P. Hannigan, N. Pinet, S. Castonguay, P. Giles and A. Hamblin  
823 (2011). "Geological setting and resource potential of conventional petroleum plays in

- 824 Paleozoic basins in eastern Canada." *Bulletin of Canadian Petroleum Geology* 59(1): 54-  
825 84.
- 826
- 827 Dulu, O. G. (1999). "Computer axial tomography in geosciences: an overview." *Earth-  
828 Science Reviews* 48(4): 265-281.
- 829
- 830 Freire-Gormaly, M., J. S. Ellis, A. Bazylak and H. L. MacLean (2015). "Comparing  
831 thresholding techniques for quantifying the dual porosity of Indiana Limestone and Pink  
832 Dolomite." *Microporous and Mesoporous Materials* 207: 84-89.
- 833
- 834 Fusi, N. and J. Martinez-Martinez (2013). "Mercury porosimetry as a tool for improving  
835 quality of micro-CT images in low porosity carbonate rocks." *Engineering Geology* 166:  
836 272-282.
- 837
- 838 Galaup, S., Y. Liu and A. Cerepi (2012). "New integrated 2D–3D physical method to  
839 evaluate the porosity and microstructure of carbonate and dolomite porous system."  
840 *Microporous and Mesoporous Materials* 154: 175-186.
- 841
- 842 Gasaway, C., M. Mastalerz, F. Krause, C. Clarkson and C. Debuhr (2018). "Application  
843 of micro-FTIR mapping and SEM to study compositional heterogeneity of siltstones:  
844 Example from the Late Devonian–Early Mississippian Middle Bakken Member." *Journal  
845 of Microscopy* 269(3): 195-211.
- 846
- 847 Geiger, J., Z. Hunyadfalvi and P. Bogner (2009). "Analysis of small-scale heterogeneity  
848 in clastic rocks by using computerized X-ray tomography (CT)." *Engineering Geology*  
849 103(3-4): 112-118.
- 850
- 851 Goldberg, D. S., D. V. Kent and P. E. Olsen (2010). "Potential on-shore and off-shore  
852 reservoirs for CO<sub>2</sub> sequestration in Central Atlantic magmatic province basalts."  
853 *Proceedings of the National Academy of Sciences* 107(4): 1327-1332.
- 854
- 855 Grader, A., M. Balzarini, F. Radaelli, G. Capasso and A. Pellegrino (2000). "Fracture-  
856 matrix flow: Quantification and visualization using X-Ray computerized tomography."  
857 Washington DC American Geophysical Union Geophysical Monograph Series 122: 157-  
858 168.
- 859
- 860 Hart, D. J. and H. F. Wang (1995). "Laboratory measurements of a complete set of  
861 poroelastic moduli for Berea sandstone and Indiana limestone." *Journal of Geophysical  
862 Research: Solid Earth* 100(B9): 17741-17751.

- 863  
864 Hartmann, A., R. Pechnig and C. Clauser (2008). "Petrophysical analysis of regional-  
865 scale thermal properties for improved simulations of geothermal installations and basin-  
866 scale heat and fluid flow." *International Journal of Earth Sciences* 97(2): 421-433.
- 867  
868 Helliwell, J. R., C. J. Sturrock, K. M. Grayling, S. R. Tracy, R. J. Flavel, I. M. Young, W.  
869 R. Whalley and S. J. Mooney (2013). "Applications of X-ray computed tomography for  
870 examining biophysical interactions and structural development in soil systems: a review."  
871 *European Journal of Soil Science* 64(3): 279-297.
- 872  
873 Holder, J., J. E. Olson and Z. Philip (2001). "Experimental determination of subcritical  
874 crack growth parameters in sedimentary rock." *Geophysical Research Letters* 28(4): 599-  
875 602.
- 876  
877 Honarpour, M., V. Cromwell, D. Hatton and R. Satchwell (1985). Reservoir rock  
878 descriptions using computed tomography (CT). SPE Annual Technical Conference and  
879 Exhibition, Society of Petroleum Engineers.
- 880  
881 Hopmans, J., T. Vogel and P. D. Koblik (1992). X-ray Tomography of Soil Water  
882 Distribution in One-Step Outflow Experiments.
- 883  
884 Hove, A., J. Ringen and P. Read (1987). "Visualization of laboratory corefloods with the  
885 aid of computerized tomography of X-rays." *SPE Reservoir Engineering* 2(02): 148-154.
- 886  
887 Islam, A., S. Chevalier and M. Sassi (2018). "Structural characterization and numerical  
888 simulations of flow properties of standard and reservoir carbonate rocks using micro-  
889 tomography." *Computers & Geosciences* 113: 14-22.
- 890  
891 Jackson, S. J., S. Agada, C. A. Reynolds and S. Krevor (2018). "Characterizing drainage  
892 multiphase flow in heterogeneous sandstones." *Water Resources Research* 54(4): 3139-  
893 3161.
- 894  
895 Jussiani, E. I. and C. R. Appoloni (2015). "Effective atomic number and density  
896 determination of rocks by X-ray microtomography." *Micron* 70: 1-6.
- 897  
898 Karacan, C., A. Grader and P. Halleck (2003). "Evaluation of local porosity changes in  
899 limestone samples under triaxial stress field by using X-ray computed tomography."  
900 Geological Society, London, Special Publications 215(1): 177-189.
- 901

- 902 Kato, M., M. Takahashi, S. Kawasaki, T. Mukunoki and K. Kaneko (2013). "Evaluation  
903 of porosity and its variation in porous materials using microfocus X-ray computed  
904 tomography considering the partial volume effect." *Materials Transactions* 54(9): 1678-  
905 1685.
- 906  
907 Ketcham, R. A. and W. D. Carlson (2001). "Acquisition, optimization and interpretation  
908 of X-ray computed tomographic imagery: applications to the geosciences." *Computers &  
909 Geosciences* 27(4): 381-400.
- 910  
911 Ketcham, R. A. and G. J. Iturrino (2005). "Nondestructive high-resolution visualization  
912 and measurement of anisotropic effective porosity in complex lithologies using high-  
913 resolution X-ray computed tomography." *Journal of Hydrology* 302(1-4): 92-106.
- 914  
915 Krause, M., S. Krevor and S. M. Benson (2013). "A Procedure for the Accurate  
916 Determination of Sub-Core Scale Permeability Distributions with Error Quantification."  
917 *Transport in porous media* 98(3): 565-588.
- 918  
919 Krause, M. H. and S. M. Benson (2015). "Accurate determination of characteristic  
920 relative permeability curves." *Advances in Water Resources* 83: 376-388.
- 921  
922 Krevor, S. C. M., R. Pini, L. Zuo and S. M. Benson (2012). "Relative permeability and  
923 trapping of CO<sub>2</sub> and water in sandstone rocks at reservoir conditions." *Water Resources  
924 Research* 48(2).
- 925  
926 Kukkonen, I. T. and S. Peltoniemi (1998). "Relationships between thermal and other  
927 petrophysical properties of rocks in Finland." *Physics and Chemistry of the Earth* 23(3):  
928 341-349.
- 929  
930 Laird, A. and J. Putnam (1959). "Three component saturation in porous media by x-ray  
931 techniques." *Petroleum Transactions, AIME* 216: 216-220.
- 932  
933 Lavoie, D. and P.-A. Bourque (2001). "The history of hydrocarbon exploration in the  
934 Silurian-Devonian Gaspé Belt: 100 years of modest success." *Bulletin of Canadian  
935 Petroleum Geology* 49(2): 180-185.
- 936  
937 Lavoie, D. and G. Chi (2010). "Lower Paleozoic foreland basins in eastern Canada:  
938 tectono-thermal events recorded by faults, fluids and hydrothermal dolomites." *Bulletin  
939 of Canadian Petroleum Geology* 58(1): 17-35.
- 940

- 941 Lavoie, D. and C. Morin (2004). "Hydrothermal dolomitization in the Lower Silurian  
942 Sayabec Formation in northern Gaspé-Matapédia (Québec): Constraint on timing of  
943 porosity and regional significance for hydrocarbon reservoirs." *Bulletin of Canadian  
944 Petroleum Geology* 52(3): 256-269.
- 945  
946 Lavoie, D., N. Pinet, J. Dietrich, P. Hannigan, S. Castonguay, A. P. Hamblin and P. Giles  
947 (2009). *Petroleum Resource Assessment: Paleozoic Succession of the St. Lawrence  
948 Platform and Appalachians of Eastern Canada*, Geological Survey of Canada: 275.
- 949  
950 Lindquist, S. J. (1988). "Practical characterization of eolian reservoirs for development:  
951 Nugget Sandstone, Utah—Wyoming thrust belt." *Sedimentary Geology* 56(1): 315-339.
- 952  
953 Lopez, O., C. Berg, L. Rennan, G. Digranes, T. Forest, A. Kristoffersen and B. Boklepp  
954 (2016). Quick Core Assessment from CT Imaging: from Petrophysical Properties to Log  
955 Evaluation. International Symposium of the Society of Core Analysts, Snomass, CO,  
956 paper SCA2016-031.
- 957  
958 Lucia, F. J. (2007). *Carbonate reservoir characterization: An integrated approach*,  
959 Springer Science & Business Media.
- 960  
961 Martin, R. J. (1968). The effect of pore pressure on the strength of low porosity  
962 crystalline rocks, Massachusetts Institute of Technology.
- 963  
964 MathWorks (2018). "Image Processing Toolbox: User's Guide." Retrieved November 30,  
965 2018, from [https://www.mathworks.com/help/pdf\\_doc/images/images\\_tb.pdf](https://www.mathworks.com/help/pdf_doc/images/images_tb.pdf).
- 966  
967 Meakin, P. and A. M. Tartakovsky (2009). "Modeling and simulation of pore-scale  
968 multiphase fluid flow and reactive transport in fractured and porous media." *Reviews of  
969 Geophysics* 47(3).
- 970  
971 Mees, F., R. Swennen, M. Van Geet and P. Jacobs (2003). "Applications of X-ray  
972 computed tomography in the geosciences." *Geological Society, London, Special  
973 Publications* 215(1): 1-6.
- 974  
975 Morgan, F., J. McDowell and E. Doty (1950). "Improvements in the X-ray saturation  
976 technique of studying fluid flow." *Journal of Petroleum Technology* 2(7): 183-194.
- 977  
978 Musselman, J. A. (1967). An experimental investigation of indexed indentation of rock.  
979 Houston, Texas, Rice University. MSc: 86.

- 980  
981 Newton, T. and D. Potts (1981). "Technical aspects of computed tomography."  
982 Radiology of the skull and brain 5: 3853-4419.
- 983  
984 Okabe, H. and M. J. Blunt (2007). "Pore space reconstruction of vuggy carbonates using  
985 microtomography and multiple-point statistics." Water Resources Research 43(12).
- 986  
987 Pak, T., I. B. Butler, S. Geiger, M. I. van Dijke, Z. Jiang and R. Surmas (2016).  
988 "Multiscale pore-network representation of heterogeneous carbonate rocks." Water  
989 Resources Research 52(7): 5433-5441.
- 990  
991 Perrin, J.-C. and S. Benson (2010a). "An experimental study on the influence of sub-core  
992 scale heterogeneities on CO<sub>2</sub> distribution in reservoir rocks." Transport in porous media  
993 82(1): 93-109.
- 994  
995 Perrin, J.-C. and S. Benson (2010b). "An experimental study on the influence of sub-core  
996 scale heterogeneities on CO<sub>2</sub> distribution in reservoir rocks." Transport in porous media  
997 82(1): 93-109.
- 998  
999 Pini, R., S. C. M. Krevor and S. M. Benson (2012). "Capillary pressure and heterogeneity  
1000 for the CO<sub>2</sub>/water system in sandstone rocks at reservoir conditions." Advances in Water  
1001 Resources 38: 48-59.
- 1002  
1003 Pini, R. and C. Madonna (2016). "Moving across scales: a quantitative assessment of X-  
1004 ray CT to measure the porosity of rocks." Journal of Porous Materials 23(2): 325-338.
- 1005  
1006 Rao, C. R., C. R. Rao, M. Statistiker, C. R. Rao and C. R. Rao (1973). Linear statistical  
1007 inference and its applications, Wiley New York.
- 1008  
1009 Schembre, J. and A. Kovscek (2003). "A technique for measuring two-phase relative  
1010 permeability in porous media via X-ray CT measurements." Journal of petroleum science  
1011 and engineering 39(1-2): 159-174.
- 1012  
1013 Schindelin, J., I. Arganda-Carreras, E. Frise, V. Kaynig, M. Longair, T. Pietzsch, S.  
1014 Preibisch, C. Rueden, S. Saalfeld and B. Schmid (2012). "Fiji: an open-source platform  
1015 for biological-image analysis." Nature methods 9(7): 676.
- 1016  
1017 Schmidt, R. A. and C. W. Huddle (1977). "Effect of confining pressure on fracture  
1018 toughness of Indiana limestone." International Journal of Rock Mechanics and Mining  
1019 Sciences & Geomechanics Abstracts 14(5): 289-293.

- 1020  
1021 Shi, J.-Q., Z. Xue and S. Durucan (2009). "History matching of CO<sub>2</sub> core flooding CT  
1022 scan saturation profiles with porosity dependent capillary pressure." *Energy Procedia*  
1023 1(1): 3205-3211.
- 1024  
1025 Simjoo, M., Y. Dong, A. Andrianov, M. Talanana and P. Zitha (2013). "CT scan study of  
1026 immiscible foam flow in porous media for enhancing oil recovery." *Industrial &*  
1027 *Engineering Chemistry Research* 52(18): 6221-6233.
- 1028  
1029 Simjoo, M. and P. L. Zitha (2018). "New Insight into Immiscible Foam for Enhancing  
1030 Oil Recovery." *Flow and Transport in Subsurface Environment*: 91-115.
- 1031  
1032 Sok, R. M., M. A. Knackstedt, T. Varslot, A. Ghous, S. Latham and A. P. Sheppard  
1033 (2010). "Pore scale characterization of carbonates at multiple scales: Integration of  
1034 Micro-CT, BSEM, and FIBSEM." *Petrophysics* 51(06).
- 1035  
1036 Soltani, A., M. Le Ravalec-Dupin and M. Fourar (2009). "An experimental method for  
1037 one dimensional permeability characterization of heterogeneous porous media at the core  
1038 scale." *Transport in porous media* 77(1): 1-16.
- 1039  
1040 Taud, H., R. Martinez-Angeles, J. Parrot and L. Hernandez-Escobedo (2005). "Porosity  
1041 estimation method by X-ray computed tomography." *Journal of petroleum science and*  
1042 *engineering* 47(3): 209-217.
- 1043  
1044 Tilke, P. G., D. Allen and A. Gyllensten (2006). "Quantitative Analysis of Porosity  
1045 Heterogeneity: Application of Geostatistics to Borehole Images." *Mathematical Geology*  
1046 38(2): 155-174.
- 1047  
1048 Van Geet, M., D. Lagrou and R. Swennen (2003). "Porosity measurements of  
1049 sedimentary rocks by means of microfocus X-ray computed tomography ( $\mu$ CT)."  
1050 *Geological Society, London, Special Publications* 215(1): 51-60.
- 1051  
1052 Van Geet, M. and R. Swennen (2001). "Quantitative 3D fracture analysis by means of  
1053 microfocus X-ray Computer Tomography ( $\mu$ CT): An example from coal." *Geophysical*  
1054 *Research Letters* 28(17): 3333-3336.
- 1055  
1056 Vaz, C. M. P., M. Tuller, P. R. O. Lasso and S. Crestana (2014). New perspectives for the  
1057 application of high-resolution benchtop X-ray microCT for quantifying void, solid and  
1058 liquid phases in soils. *Application of soil physics in environmental analyses*, Springer:  
1059 261-281.

- 1060  
1061 Victor, R. A., M. Prodanović and C. Torres-Verdín (2017). "Monte Carlo Approach for  
1062 Estimating Density and Atomic Number From Dual-Energy Computed Tomography  
1063 Images of Carbonate Rocks." *Journal of Geophysical Research: Solid Earth* 122(12):  
1064 9804-9824.
- 1065  
1066 Vinegar, H. J. and S. L. Wellington (1987). "Tomographic imaging of three-phase flow  
1067 experiments." *Review of Scientific Instruments* 58(1): 96-107.
- 1068  
1069 Walls, J. and M. Armbruster (2012). "Shale reservoir evaluation improved by dual energy  
1070 X-Ray CT imaging." *Journal of Petroleum Technology* 64(11): 28-32.
- 1071  
1072 Wang, S. Y., S. Ayril and C. C. Gryte (1984). "Computer-assisted tomography for the  
1073 observation of oil displacement in porous media." *Society of Petroleum Engineers*  
1074 *Journal* 24(01): 53-55.
- 1075  
1076 Wellington, S. L. and H. J. Vinegar (1987). "X-ray computerized tomography." *Journal*  
1077 *of Petroleum Technology* 39(08): 885-898.
- 1078  
1079 Wildenschild, D. and A. P. Sheppard (2013). "X-ray imaging and analysis techniques for  
1080 quantifying pore-scale structure and processes in subsurface porous medium systems."  
1081 *Advances in Water Resources* 51: 217-246.
- 1082  
1083 Wildenschild, D., C. Vaz, M. Rivers, D. Rikard and B. Christensen (2002). "Using X-ray  
1084 computed tomography in hydrology: systems, resolutions, and limitations." *Journal of*  
1085 *Hydrology* 267(3-4): 285-297.
- 1086  
1087 Winkler, K. W. (1983). "Frequency dependent ultrasonic properties of high porosity  
1088 sandstones." *Journal of Geophysical Research: Solid Earth* 88(B11): 9493-9499.
- 1089  
1090 Withjack, E. (1988). "Computed tomography for rock-property determination and fluid-  
1091 flow visualization." *SPE formation evaluation* 3(04): 696-704.
- 1092  
1093 Xiong, Q., T. G. Baychev and A. P. Jivkov (2016). "Review of pore network modelling  
1094 of porous media: Experimental characterisations, network constructions and applications  
1095 to reactive transport." *Journal of contaminant hydrology* 192: 101-117.
- 1096  
1097 Yuen, H., J. Princen, J. Illingworth and J. Kittler (1990). "Comparative study of Hough  
1098 transform methods for circle finding." *Image and vision computing* 8(1): 71-77.

1099

1100 Zaretskiy, Y., S. Geiger, K. Sorbie and M. Förster (2010). "Efficient flow and transport  
1101 simulations in reconstructed 3D pore geometries." *Advances in Water Resources* 33(12):  
1102 1508-1516.

1103

1104

ACCEPTED MANUSCRIPT

1105 **FIGURES CAPTIONS**

1106 **TAB. 1** List of references samples used for the present work. In the sample name, the  
1107 petroleum core sample provider is indicated, with K standing for Kocurek Industries Inc  
1108 and C standing for Cleveland Quarries. All basic samples measurements were performed  
1109 at the LOG, using a digital caliper and a precision scale. BE stands for Berea sandstone;  
1110 SC stands for Scioto sandstone; BO stands for Boise sandstone, NU stands for Nugget  
1111 sandstone; IN stands for Indiana sandstone; CA stands for Carthage Marble (= Burlington  
1112 Limestone); GE stands for Guelph dolomite; SI stands for Silurian dolomite.

1113 **TAB. 2** Comparison of methods used in the present work to estimate porosity.

1114 **TAB. 3** Summary of CT-scanner parameters values for both acquisition and reconstitution  
1115 stages. kV stands for kilovoltage, mAs for milliampere-second, F.O.V. for field of view,  
1116 and HU for Hounsfield Unit.

1117 **TAB. 4** Summary of results for reference core samples. The absolute error (AE)  
1118 corresponds to the difference between the porosity calculated using the improved CT-  
1119 scan methodology and the porosity measured using the conventional gas porosimeter  
1120 IHAP.

1121 **TAB. 5** Summary of results for silurian core samples.

1122 **FIG. 1** Range of porosity tested for this work. Reference core samples correspond to eight  
1123 different lithologies commonly used as test material in the petroleum industry, and cover  
1124 a large range of porosity (2-5 to 28 %), namely Berea, Scioto, Nugget and Boise  
1125 sandstones (SST), Indiana and Burlington limestones (LST), and Silurian and Guelph  
1126 dolomites. For each lithology type, an expected porosity or porosity range was given by  
1127 the vendor Kocurek Industries and these values are reported here.

1128 **FIG. 2** Petrographic attributes of reference core material. (A) Microphotograph of  
1129 medium-grained Nugget sandstone sample, with moderate sorting and well-rounded  
1130 grains. (B) Microphotograph of medium to coarse-grained Boise sandstone sample, with  
1131 poor sorting. Quartz grains are angular (C-D) Microphotographs of fine-grained, well  
1132 sorted Scioto sandstone. Quartz grains are subangular. (E) Microphotograph of Carthage  
1133 marble limestone. This limestone is a well cemented, fossiliferous limestone with  
1134 moderate to poor sorting. (F) Microphotograph of homogeneous fine grained Silurian  
1135 dolostone within the Sayabec Formation.

1136 **FIG. 3.** Simplified geological map of the Témiscouata area in eastern Quebec (Canada)  
1137 with the location of the Massé No 1 well (black star). The yellow star locates the position  
1138 of an exhumed hydrocarbon field hosted in hydrothermal dolomite (HTD). The  
1139 stratigraphic column to the left locates the Sayabec - Val Brillant interval deposited at the  
1140 end of the first shallowing event (S1) and onset of the first deepening event (D1) in the  
1141 Gaspé Belt. Stratigraphic details and basin evolution are found in Bourque et al. (1995).

1142

1143 **FIG. 4.** (A) Macrophotograph of silurian core interval used for this study. These  
1144 continuous 4.5 meter long core section belong to the lower Silurian Sayabec Formation in  
1145 Massé No. 1 well drilled within the Massé structure (Lower St-Lawrence river area,  
1146 Québec). Core samples are 4.5 cm in diameter and their length ranges from 5 to 10 cm  
1147 (approximately). (B) Macrophotograph of five Silurian core samples, chosen to illustrate  
1148 the natural heterogeneity of this interval along depth. Each sample is briefly described  
1149 and porosity is assessed from macroscopic observations on the surface.

1150 **FIG. 5** Schematic diagram of the core flooding experimental setup for porosity  
1151 measurement. The water tank is a closed reservoir with a 4 L total volume. To  
1152 accommodate meter long core section, four chamber are set in parallel.

1153 **FIG. 6** Workflow chart illustrating the successive steps involved in the present work and  
1154 separated in three groups: experiment, CT-scanning acquisition and processing.

1155 **FIG. 7** (A) Impact of noise level on porosity calculation and its uncertainty level (adopted  
1156 from Pini and Madonna (2016) ). (B) Axial CT-scans with decreasing resolution. This  
1157 illustrates how fine structures (such as fractures) could remain undetected if the  
1158 resolution is too low. The spatial resolution was then set to 0.1 x 0.1 x 0.6 mm.

1159 **FIG. 8** Statistical comparison of three gas porosity measurement techniques. (A) IHAP  
1160 versus AP-608 with  $n = 20$ , (B) IHAP versus AccuPyc with  $n = 10$ , and (C) AP-608  
1161 versus AccuPyc, with  $n = 10$ .

1162 **FIG. 9** Indiana limestone sample (IN-C-178B) with its highly irregular surface.  
1163 Macropores and core damages are abundant on the external surface which produce an  
1164 imprecise total volume calculation using caliper and could induce the outlier data point  
1165 (see Fig. 6; Fig. 9A).

1166 **FIG. 10** Statistical comparison of CT-scan porosity measurement technique against  
1167 conventional gas porosity technique (IHAP). The outlier results (white star) corresponds  
1168 to carbonate sample IN-C-178B, and was not considered for regression. For further  
1169 analyses and subsequent figures, the slope of the regression line is used as a correction  
1170 factor.

1171 **FIG. 11** Statistical comparison of CT-scan porosities against IHAP after correction. The  
1172 correction factor used (1/0.91) intends to correct beam hardening effect. The outlier  
1173 carbonate sample (IN-C-178B) and was not considered for regression.

1174 **FIG. 12** Lithology influence on the correlation between CT-scan porosity method and  
1175 conventional IHAP. Note that all data point used are corrected values. (A) Data points for  
1176 sandstones (n=14); (B) data points for limestones (n=10) and (C) data points for  
1177 dolomites (n=6). Indiana limestone outlier (IN-C-178B) was not considered for  
1178 regression.

1179 **FIG. 13** Porosity range influence on the correlation between CT-scan porosities and  
1180 conventional IHAP. Note that all data point used are corrected values. Low porosity  
1181 range is defined as porosity values lower than 15 % (n=10); and high porosity range is  
1182 defined as porosity values higher than 15% (n=19). Indiana outlier (IN-C-178B) was not  
1183 taken in consideration for regression.  $R^2$  for both ranges of porosity values reaches 0.98,  
1184 and RMSE are rather low, close to 0.5.

1185 **FIG. 14** Core diameter influence on the correlation between CT-scan porosities and  
1186 conventional IHAP, with (A) 1½” diameter core samples and (B) 1<sup>7/8</sup>” diameter core  
1187 samples.

1188 **FIG. 15** Statistical comparison of CT-scan porosities obtained with doping agent (NaI)  
1189 against IHAP porosities. Note that all data point used are corrected values. Two outlier  
1190 samples (not shown) were not considered for regression. Both outlier correspond to  
1191 Indiana limestone samples, and one of them is IN-C-178B (Fig. 8).

1192 **FIG. 16** Continuous porosity profiles obtained for a 1.8 meters thick section of the lower  
1193 Silurian hydrothermal dolomites. The average porosity for this entire section is 3.38%.

1194 The continuous porosity values are compared to discrete helium gas porosity values  
1195 obtained at the AGAT laboratories, and CT-scan porosity value average per subsamples  
1196 (CSI-3, CSI-6, CSI-10, CSI-12 and CSI-16). The different profiles were plotted using IP  
1197 software. A bell (Gaussian) filter was applied to the mean CT-scan porosity values. HI  
1198 (heterogeneity index) and CV (coefficient of variation) parameters are adopted from  
1199 Caliskan and Shebatalhamd (2017)

1200 **FIG. 17** Examples of 2D views illustrating connected porosity matrices obtained for two  
1201 specific subsamples within the HTD interval. Greyscale indicates porosity, from 0 %  
1202 (black) to 100% (white). (A-B) correspond to coronal and sagittal mean intensity  
1203 projections views (MIP) respectively of the sample CSI-2 Sample CSI-5 MIP views are  
1204 shown in the same manner in (C-D). See Fig. 15 for samples location. Provided as  
1205 supplementary material, 360° rotation movies of these two samples were made using  
1206 Dragonfly software.

1207 **FIG. 18** Examples of coronal CT images from (A) a reference core sample, namely SI-K-  
1208 15A and from (B) one sample from the HTD interval, namely CSI-12 (see Fig. 16 for its  
1209 location along the porosity profile). Both dolomite samples have similar porosity values  
1210 obtained by IHAP, i.e. 9.5% and 9.32 % respectively (see Table 4 and 5).

Location	Number of specimen	Lithology type	Average porosity (from literature)	References
Ohio (USA)	8	Berea SST	20%	Winkler, 1983; Churcher et al., 1991; Hart and Wang, 1995; Boon et al., 2017
Utah and Wyoming (USA)	2	Nugget SST	up to 25%	Lindquist, 1988
Idaho (USA)	2	Boise SST	28-30%	Winkler, 1983
Ohio (USA)	2	Scioto SST	12%	Holder et al., 2001; Bose et al., 2014
Indiana (USA)	8	Indiana LST	13%	Musselman, 1967; Schmidt and Huddle, 1977; Churcher et al., 1991; Hart and Wang, 1995; Boon et al., 2017
Ohio (USA)	2	Carthage LST	1.5%	Musselman, 1967; Martin, 1968
Ohio (USA)	2	Silurian dolomite	14-20%	Islam et al., 2018
Ohio (USA) and Ontario (Canada)	4	Guelph dolomite	7-24%	Churcher et al., 1991

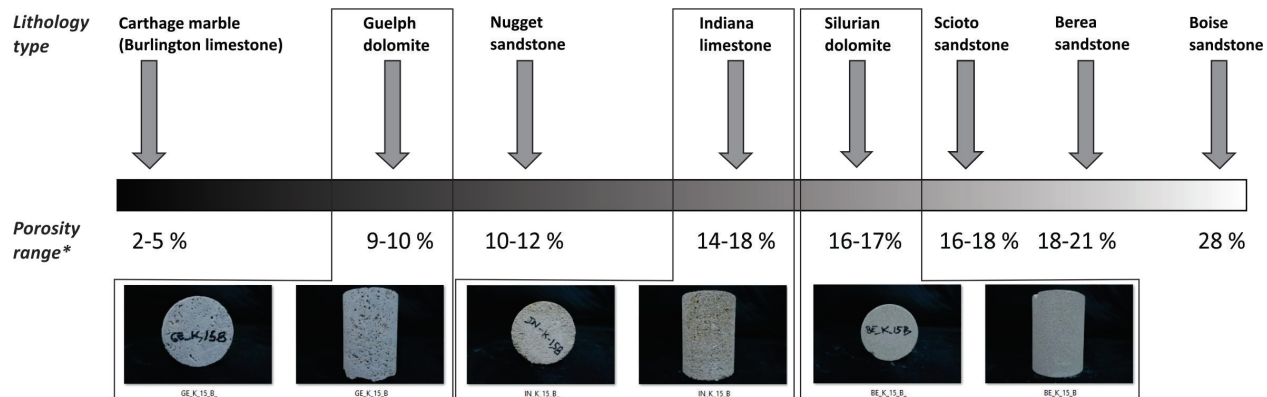
	AccuPyc	AP-608 porosimeter	AGAT Helium porosimeter	CT-scan
<b>Sample length (cm)</b>	2.54	2.54 to 10.16	2.54 to 7.62	up to 250
<b>Sample diameter (cm)</b>	2.54	2.54	2.54 or 3.81 or 5.08	up to 50
<b>Injection pressure (psi)</b>	20	200	100	<i>not applicable</i>

ACCEPTED MANUSCRIPT

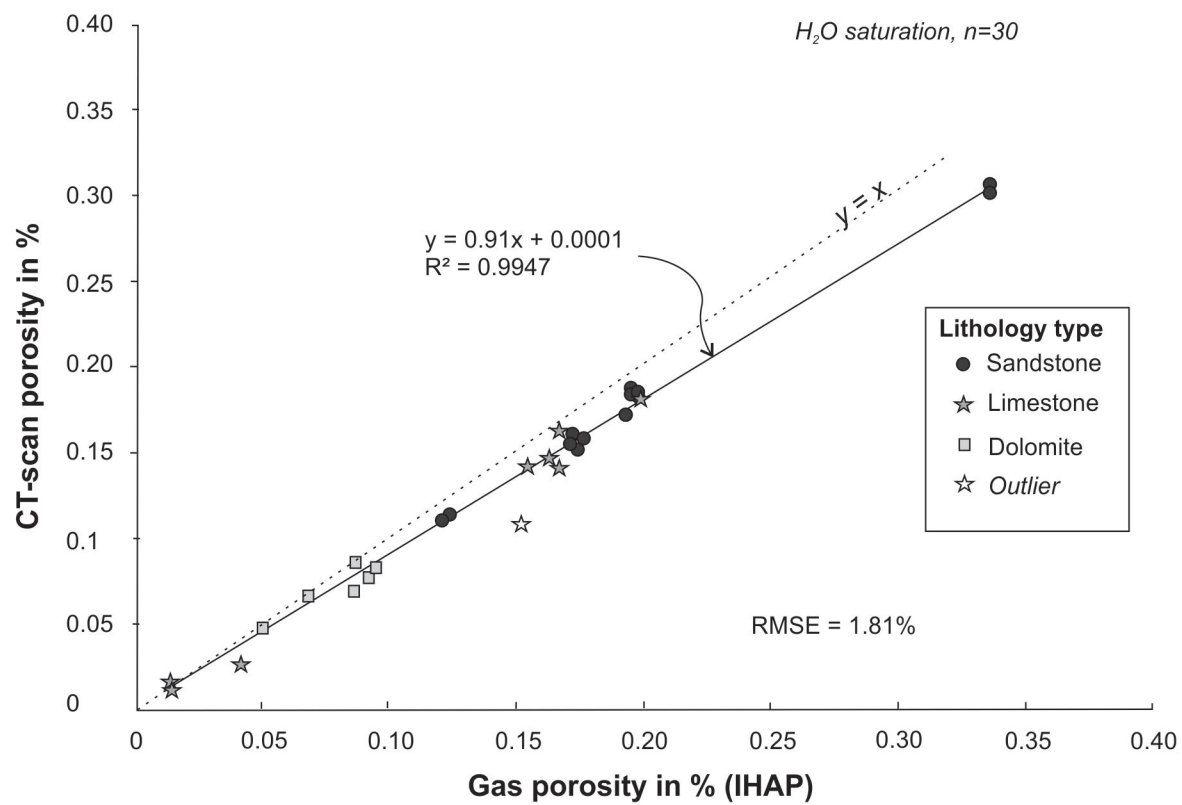
<b>Acquisition parameters</b>		
	Reference samples	Natural core samples
<b>kVp</b>	140	140
<b>mAs</b>	700	350
<b>Pitch</b>	0.55	0.55
<b>Collimation</b>	20 x 0,6 mm	20 x 0,6 mm
<b>Reconstruction parameters</b>		
	Reference samples	Natural core samples
<b>Filter</b>	H70h	H70h
<b>F.O.V</b>	60 mm	55 mm
<b>Pixels spacing</b>	0.1172 x 0.1172	0.1074 x 0.1074
<b>Slice thickness</b>	0.6 mm	0.6 mm
<b>HU scale</b>	normal	normal
<b>Focal spot</b>	1.2 mm	1.2 mm

Sample name	Sample attributes				Measured porosity (this work)					Absolute error	Reference porosity	
	Length (mm)	Diameter (mm)	Weight (g)	Lithology	AccuPyc	AP-608	IHAP	CT-scan (H2O)	CT-scan (NaI)		Littérature	Core vendor
BE_C_15_A	9.9	3.8	236.00	Berea SST	n/a	20.30%	19.80%	20.02%	n/a	0.22%	20%	18-21%
BE_C_15_B	5.2	3.8	121.70	Berea SST	20.16%	20.31%	19.80%	20.35%	17.21%	0.55%		
BE_C_178_A	74.9	4.5	287.87	Berea SST	n/a	n/a	17.10%	17.12%	n/a	0.02%		
BE_C_178_B	75.2	4.5	290.12	Berea SST	n/a	n/a	17.20%	17.71%	12.75%	0.51%		
BE_K_15_A	9.9	3.8	238.30	Berea SST	n/a	19.74%	19.30%	18.95%	n/a	0.35%		
BE_K_15_B	5.1	3.8	124.00	Berea SST	19.38%	20.25%	19.30%	18.86%	16.52%	0.44%		
BE_K_178_A	74.6	4.5	311.50	Berea SST	n/a	n/a	19.50%	20.38%	n/a	0.88%		
BE_K_178_B	75.5	4.5	315.28	Berea SST	n/a	n/a	19.50%	20.20%	16.14%	0.70%		
NU-K-15A	8.21	3.83	217.00	Nugget SST	n/a	13.27%	12.10%	12.20%	n/a	0.10%	up to 25%	10-12%
NU-K-15B	4.97	3.84	130.80	Nugget SST	13.63%	14.23%	12.30%	12.34%	10.57%	0.04%		
BO-K-15A	8.13	3.79	156.37	Boise SST	n/a	34.99%	33.60%	33.68%	n/a	0.08%	28-30%	128%
BO-K-15B	4.91	3.79	94.51	Boise SST	34.60%	34.36%	33.60%	33.19%	28.45%	0.41%		
SC-K-15A	8.13	3.82	199.80	Scioto SST	n/a	19.45%	17.40%	16.75%	n/a	0.65%	12%	16-18%
SC-K-15B	4.93	3.81	121.20	Scioto SST	18.90%	18.89%	17.60%	17.45%	14.82%	0.15%		
IN_C_15_A	9.90	3.77	248.50	Indiana LST	n/a	17.18%	16.30%	16.15%	n/a	0.15%	13%	14-18%
IN_C_15_B	5.10	3.77	127.70	Indiana LST	16.61%	17.59%	16.30%	16.04%	12.77%	0.26%		
IN_C_178_A	74.36	4.50	294.95	Indiana LST	n/a	n/a	15.40%	15.58%	n/a	0.18%		
IN_C_178_B	76.31	4.50	304.64	Indiana LST	n/a	n/a	15.20%	11.46%	10.60%	3.74%		
IN_K_15_A	9.80	3.76	233.30	Indiana LST	n/a	20.45%	19.90%	19.88%	n/a	0.02%		
IN_K_15_B	5.20	3.76	123.20	Indiana LST	18.85%	21.01%	19.90%	19.97%	15.98%	0.07%		
IN_K_178_A	74.38	4.50	325.99	Indiana LST	n/a	n/a	16.70%	17.88%	n/a	1.18%		
IN_K_178_B	75.50	4.50	331.30	Indiana LST	n/a	n/a	16.70%	15.53%	7.75%	1.17%		
CA-K-15A	8.07	3.81	242.70	Carthage LST	n/a	2.76%	1.40%	1.37%	n/a	0.03%	1.50%	2-5%
CA-K-15B	5.01	3.818	150.4	Carthage LST	2.82%	3.34%	1.40%	1.51%	0.57%	0.11%		
SI-K-15A	8.05	3.83	236.10	Silurian Dol	n/a	9.69%	9.50%	9.11%	n/a	0.39%	14-20%	16-18%
SI-K-15B	4.99	3.84	146.20	Silurian Dol	10.14%	10.09%	9.20%	8.38%	6.47%	0.82%		
GE_K_15_A	8.95	3.78	260.00	Guelph Dol	n/a	8.96%	8.60%	7.65%	n/a	0.95%	7-24%	9-10%
GE_K_15_B	5.14	3.78	147.70	Guelph Dol	8.94%	10.63%	8.70%	9.49%	7.03%	0.79%		
GE_K_178_A	66.91	4.50	355.17	Guelph Dol	n/a	n/a	5.00%	5.22%	n/a	0.22%		
GE_K_178_B	76.13	4.50	397.71	Guelph Dol	n/a	n/a	6.80%	7.32%	5.24%	0.52%		

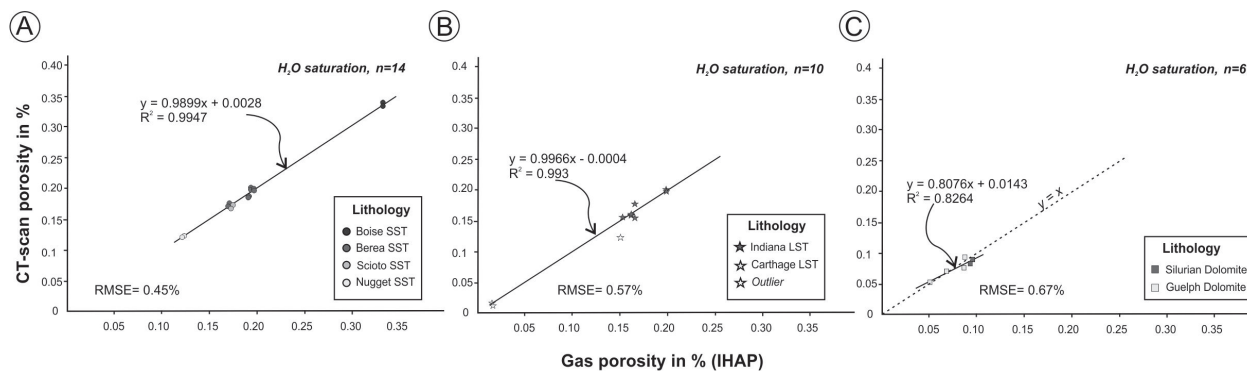
Sample name	Sample attributes		Measured porosity (this work)	
	Length (cm)	Diameter (mm)	CT-scan (H2O) corrected	IHAP
CSI-1	13.0	4.5	7.76%	n/a
CSI-2	9.0	4.5	7.03%	n/a
CSI-3	5.5	4.5	<b>2.51%</b>	<b>2.10%</b>
CSI-4	12.5	4.5	1.93%	n/a
CSI-5	11.0	4.5	2.76%	n/a
CSI-6	6.0	4.5	<b>2.42%</b>	<b>1.90%</b>
CSI-7	5.0	4.5	1.43%	n/a
CSI-8	18.0	4.5	6.82%	n/a
CSI-9	6.50	4.5	5.73%	n/a
CSI-10	7.00	4.5	<b>4.54%</b>	<b>4.20%</b>
CSI-11	17.00	4.5	3.99%	n/a
CSI-12	11.00	4.5	<b>9.36%</b>	<b>11.30%</b>
CSI-13	5.00	4.5	4.35%	n/a
CSI-14	11.00	4.5	8.89%	n/a
CSI-15	4.00	4.5	7.43%	n/a
CSI-16	6.00	4.5	<b>2.53%</b>	<b>3.00%</b>
CSI-17	4.00	4.5	3.60%	n/a
CSI-18	9.50	4.5	2.92%	n/a

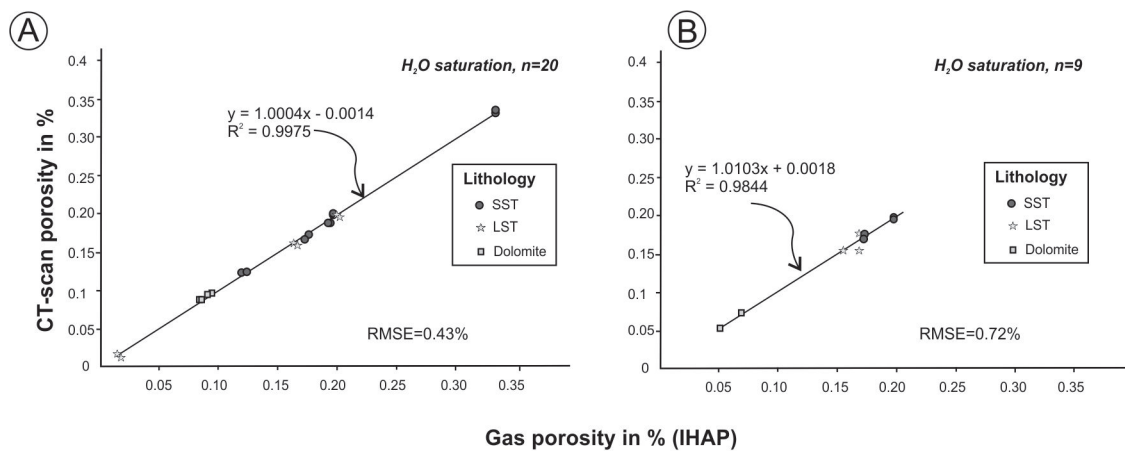


\*source Kocurek Industries Hard Rock Division (<https://kocurekindustries.com>)

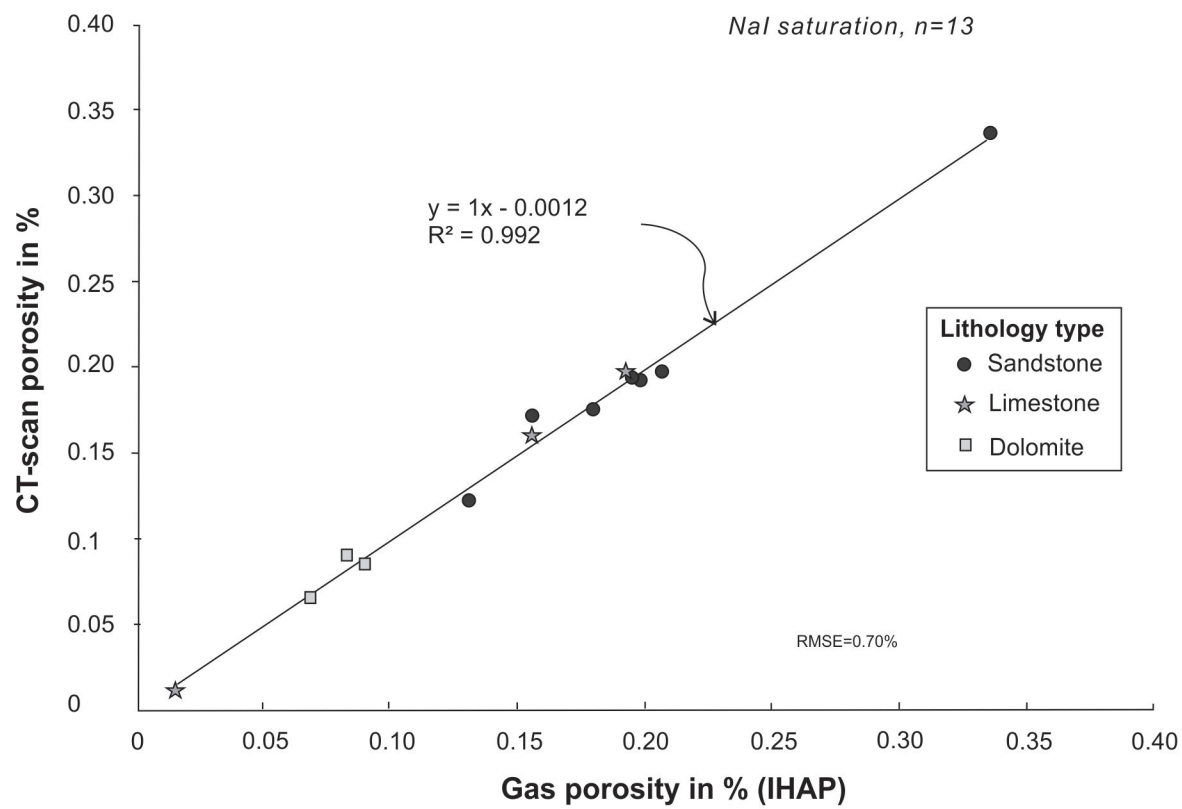


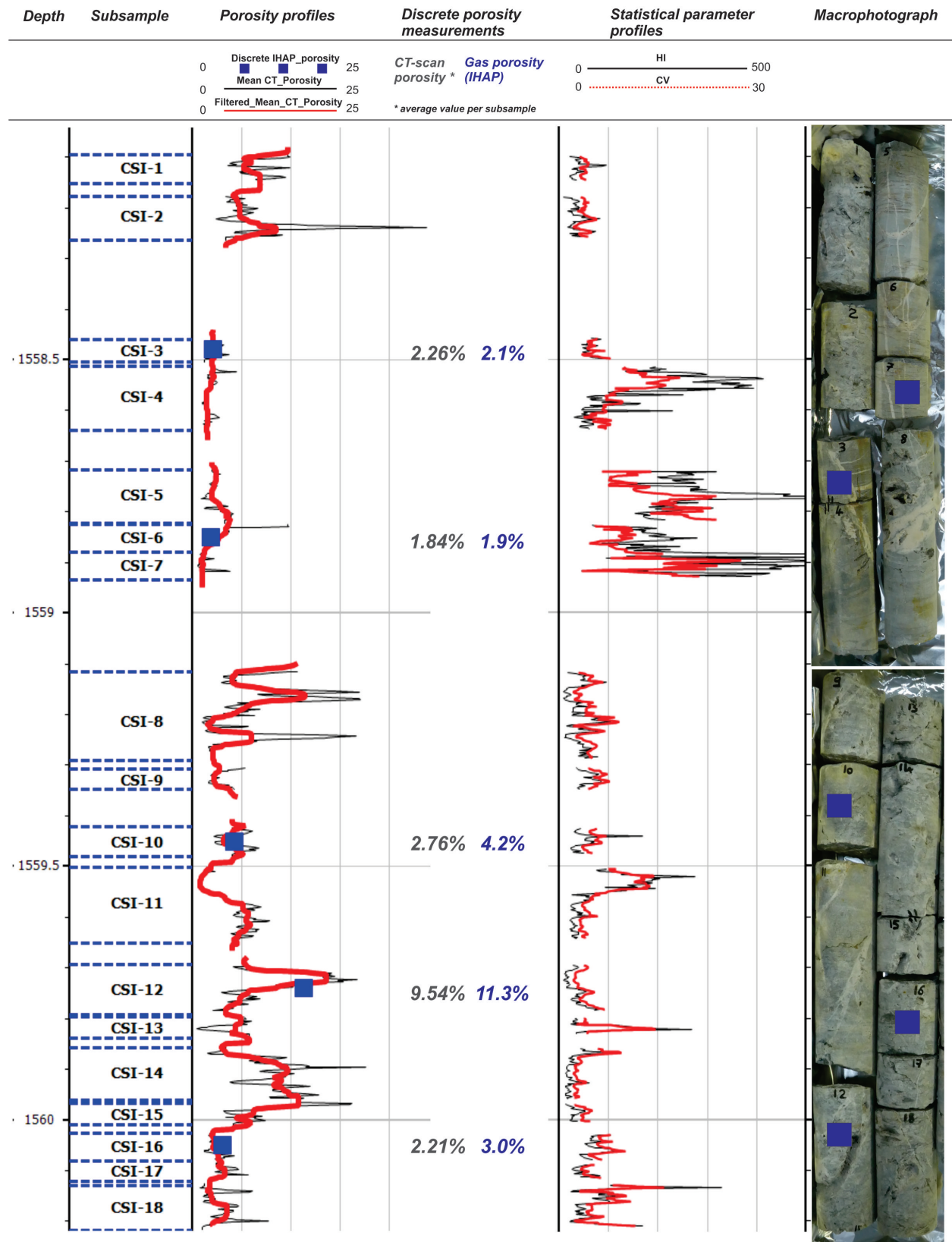


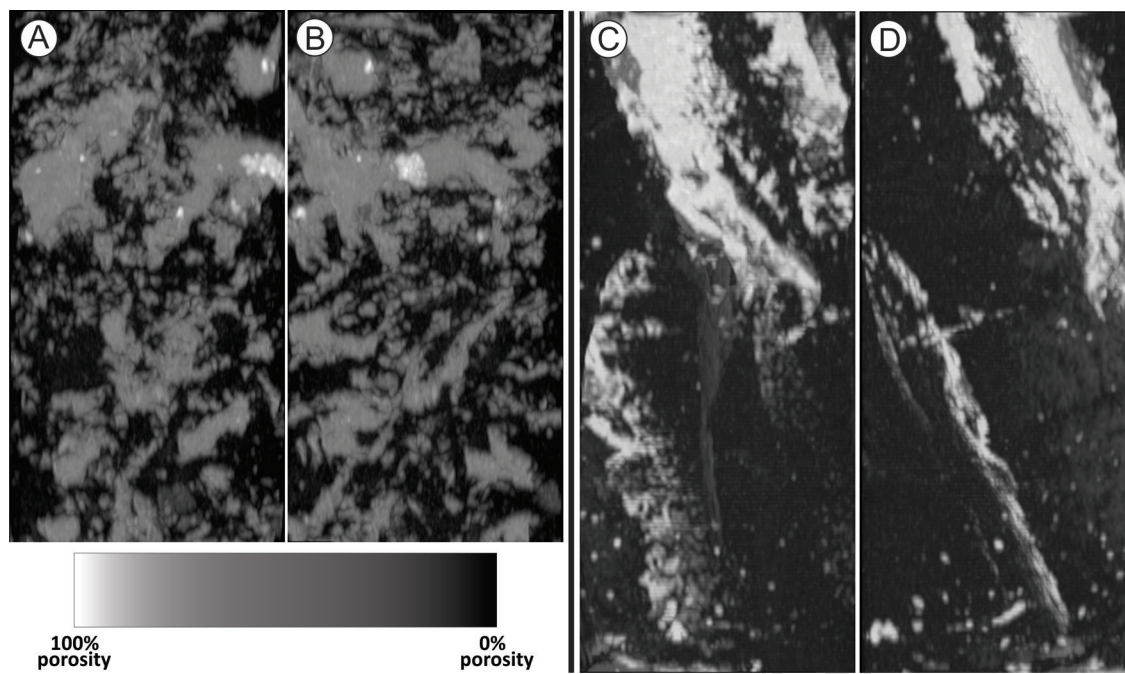


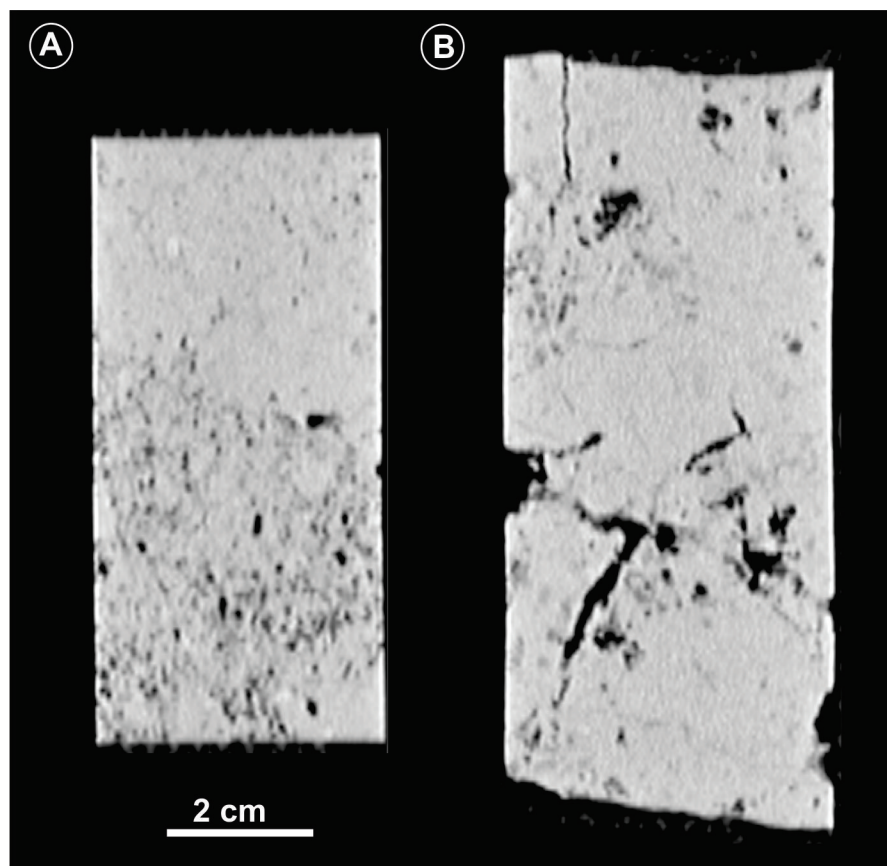


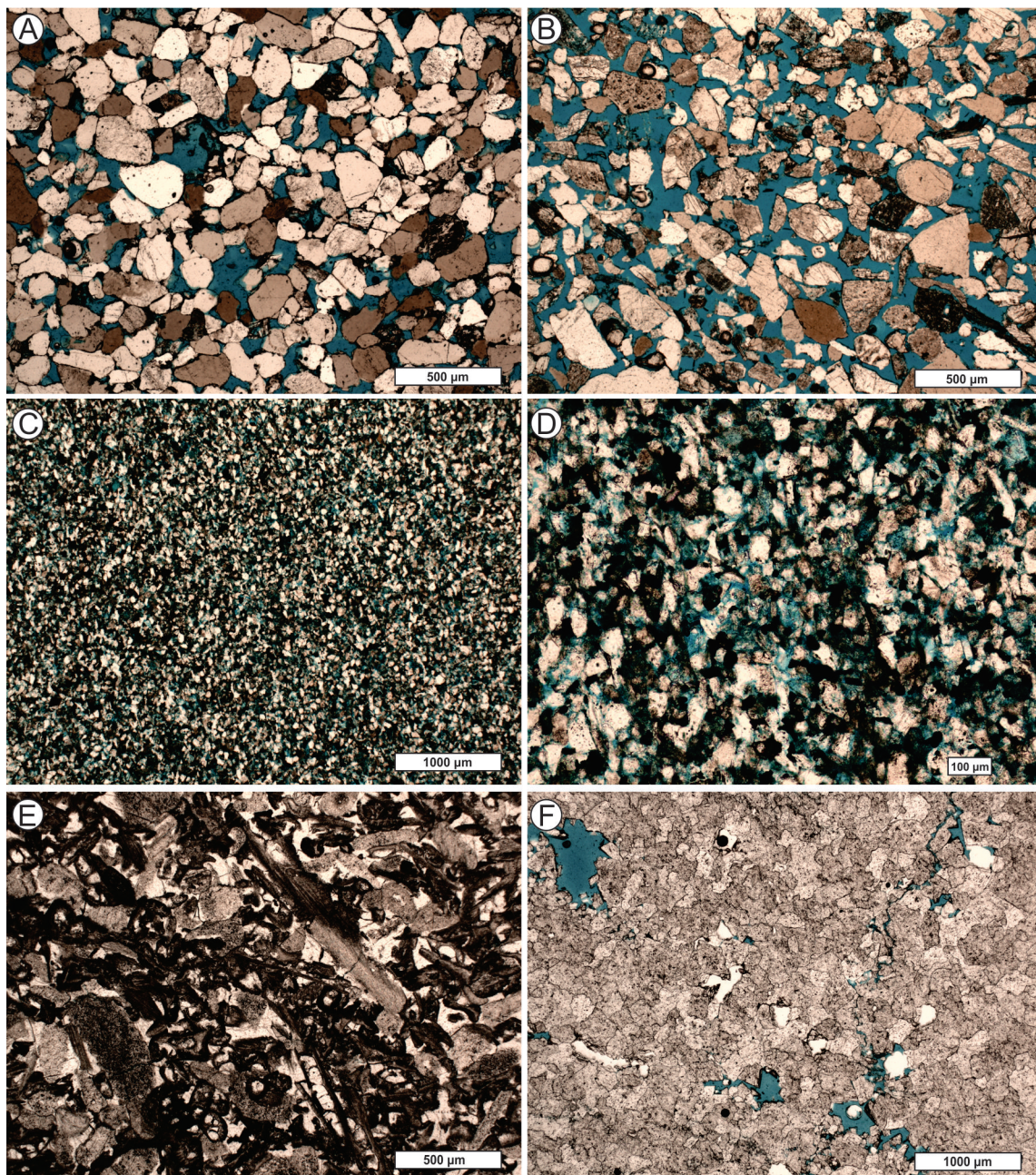


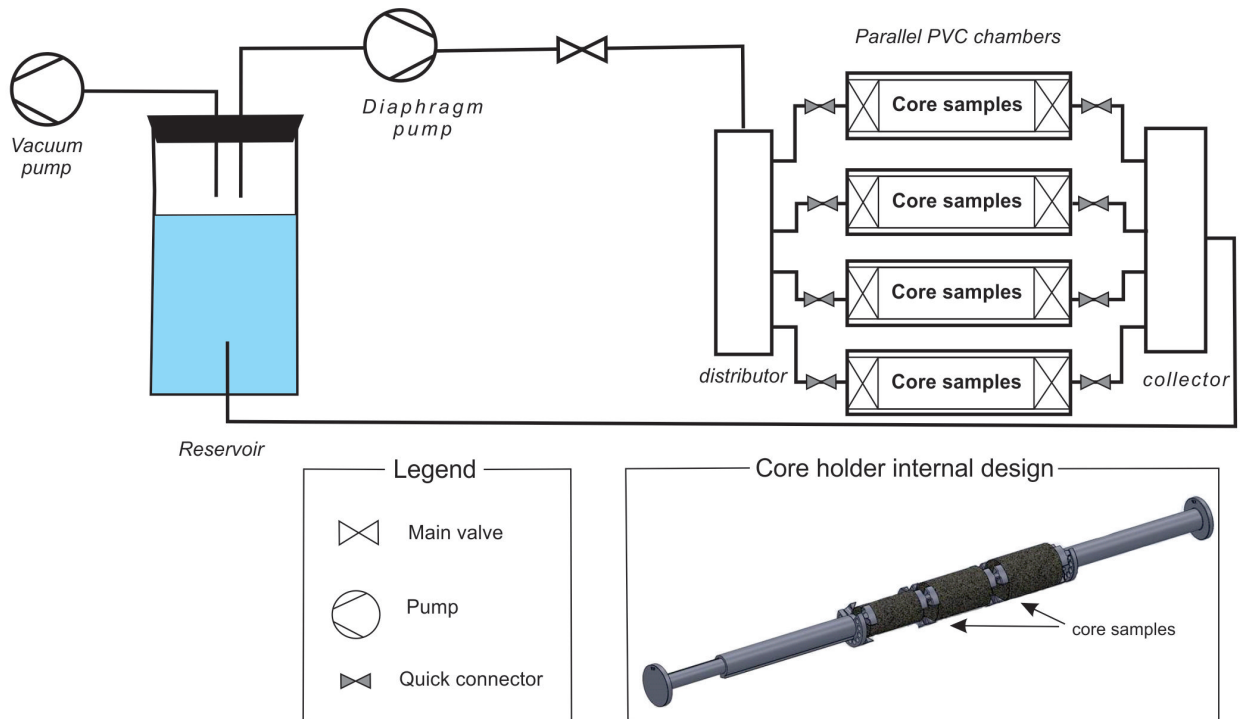


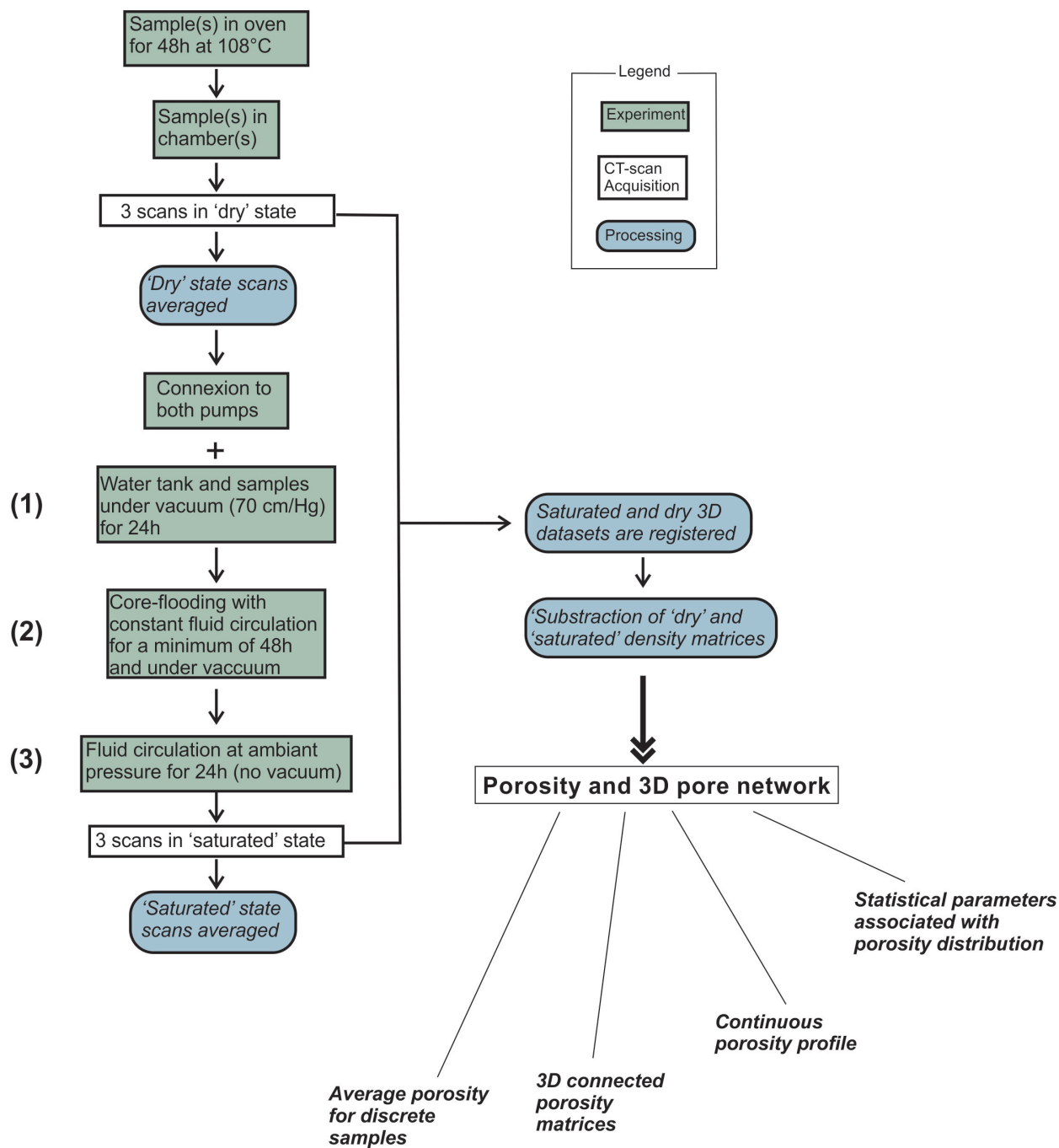


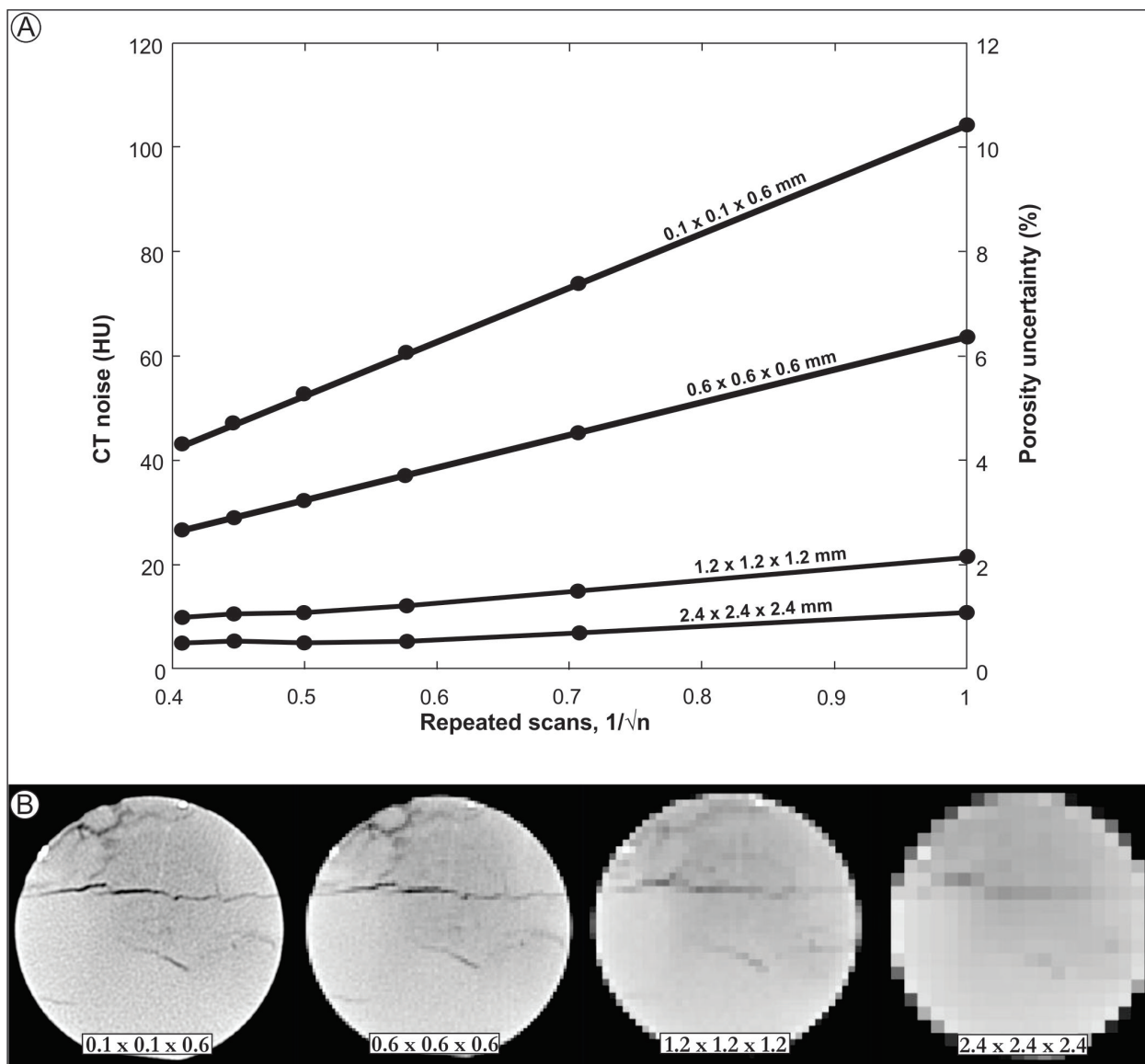


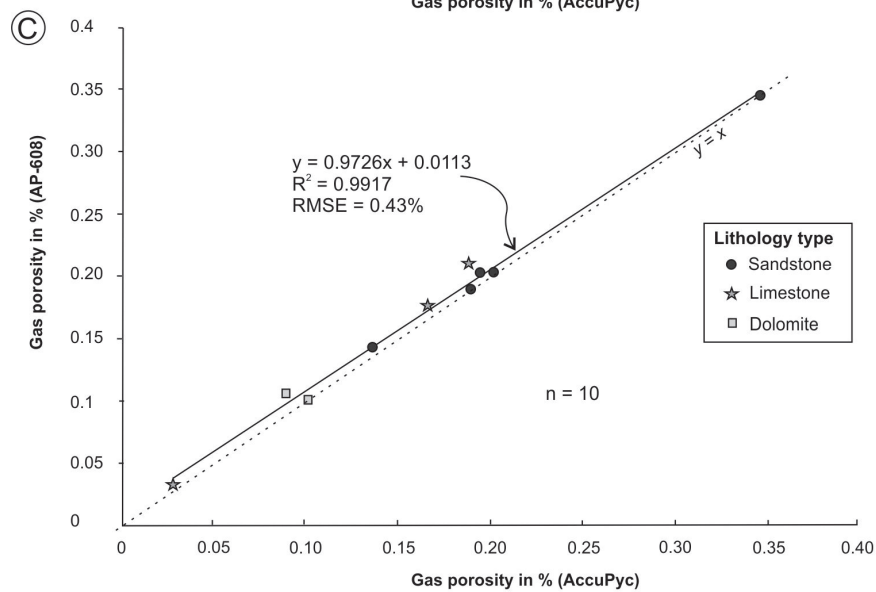
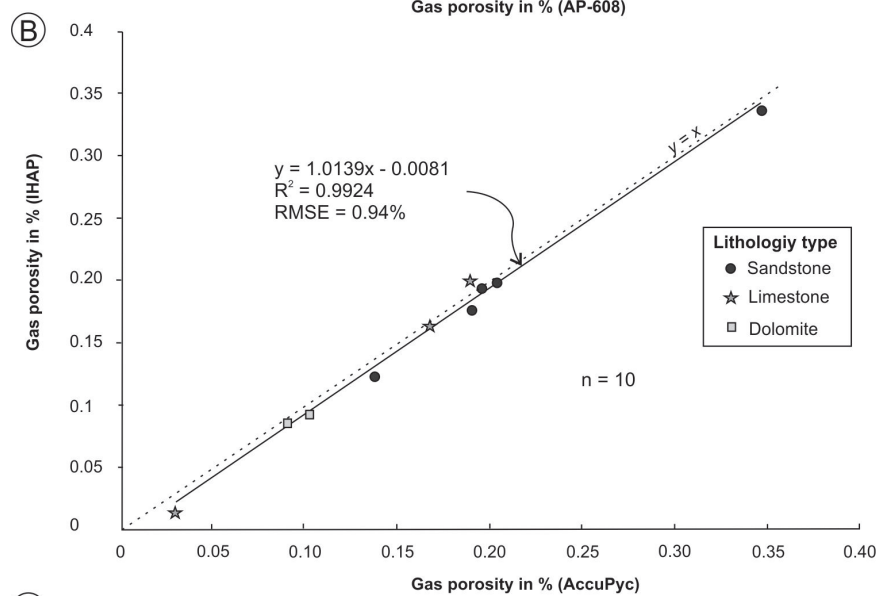
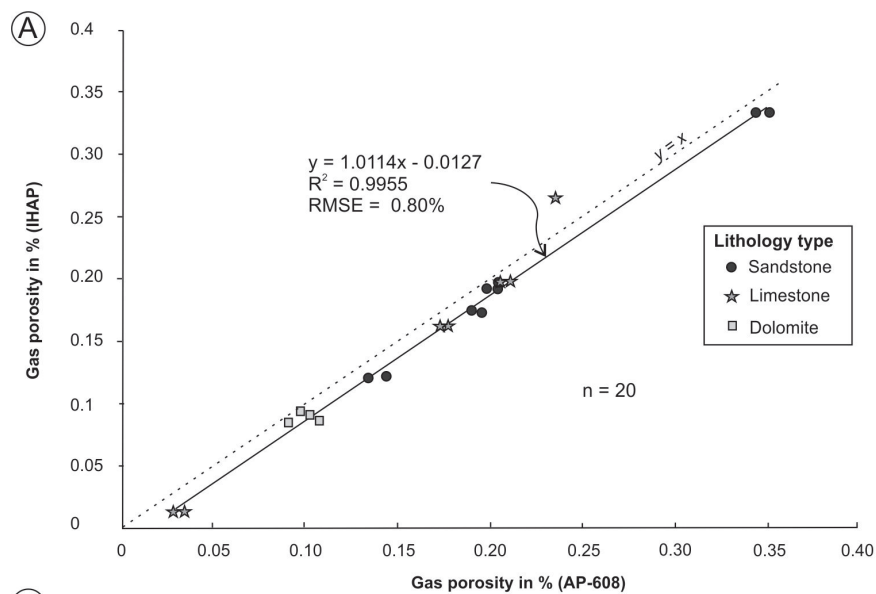


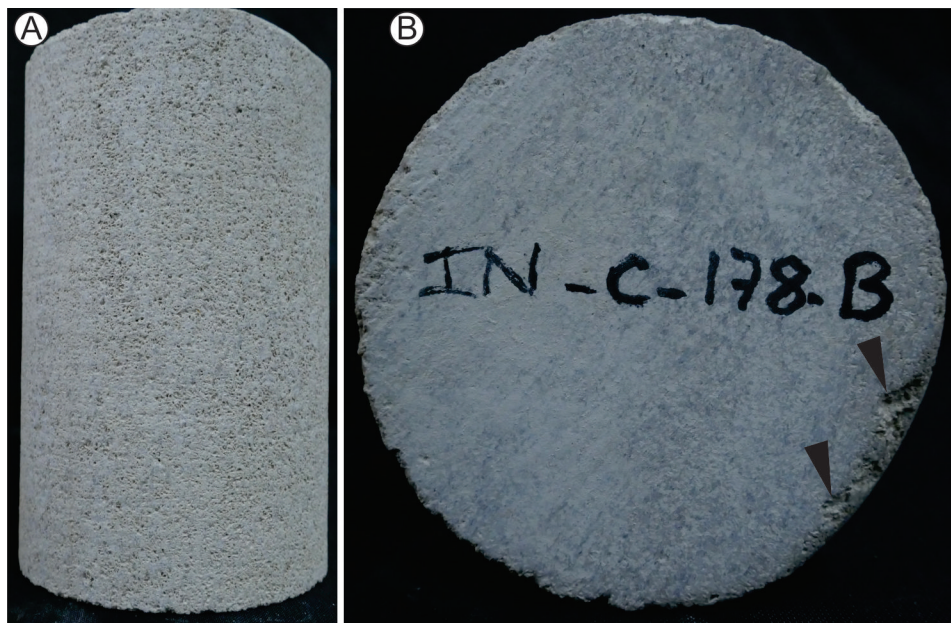


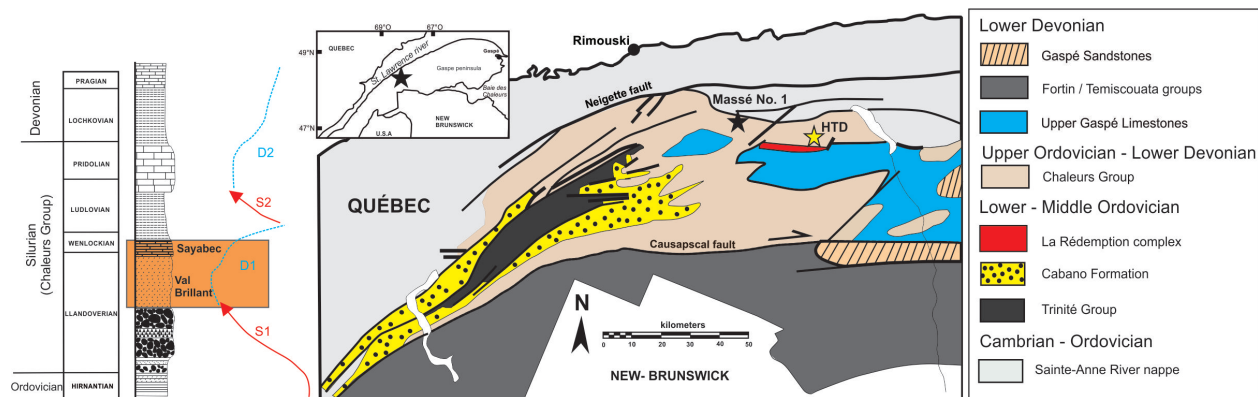












**Silurian sample #3***Description*

Fine-grained limestone with horizontal and oblique fractures and veins.

*Porosity*

Porosity was expected to be relatively low, and associated with unsealed fractures.

**Silurian sample #6***Description*

Fine-grained, laminated limestone with vertical and oblique fractures and veins.

*Porosity*

Open porosity is visible on sample surface associated with oblique fractures. However, porosity is expected to be low.

**Silurian sample #10***Description*

Massive dolomitized limestone with original depositional texture not visible at the macroscale.

*Porosity*

Thin cracks associated with visible porosity (intergranular porosity?).

**Silurian sample #12***Description*

Massive dolomitized limestone largely affected by centimetric fractures and dissolution. Original depositional texture is not preserved.

*Porosity*

Open porosity is visible on surface and associated with large, centimetric fractures.

**Silurian sample #16***Description*

Bioclastic limestone with millimetric to plurimillimetric open vugs, often associated with moldic porosity.

*Porosity*

Open porosity is visible on surface sample as dissolved molds.

ACC

**Highlights**

- (1) Combined core-flooding setup and medical-CT give porosity for heterogeneous material.
- (2) Reference core material were tested and included 7 different lithologies
- (3) The new CT methodology developed strongly correlates with conventional gas porosimetry.
- (4) 3D porosity matrices and continuous porosity profiles at submillimetric scale are produced.